HHS Public Access

Author manuscript

*Cell Host Microbe*. Author manuscript; available in PMC 2022 September 08.

Published in final edited form as:

*Cell Host Microbe*. 2021 September 08; 29(9): 1407–1420.e5. doi:10.1016/j.chom.2021.07.002.

# *Cryptosporidium* rhoptry effector protein ROP1 injected during invasion targets the host cytoskeletal modulator LMO7

**Amandine Guérin**[1], **Nathan H. Roy**[3], **Emily M. Kugler**[1], **Laurence Berry**[2], **Janis K. Burkhardt**[3], **Jung-Bum Shin**[4], **Boris Striepen**[1,†]

[1]Department of Pathobiology, School of Veterinary Medicine, University of Pennsylvania, Philadelphia, PA 19104, USA.

[2]LPHI, CNRS, Université de Montpellier, Montpellier, 34095, France.

[3]Department of Pathology and Laboratory Medicine, Children's Hospital of Philadelphia and University of Pennsylvania, Philadelphia, PA 19104, USA.

[4]Department of Neuroscience, University of Virginia, Charlottesville, VA 22908, USA.

## Abstract

The parasite *Cryptosporidium* invades and replicates in intestinal epithelial cells and is a leading cause of diarrheal disease and early childhood mortality. The molecular mechanisms that underlie infection and pathogenesis are largely unknown. Here we delineate the events of host cell invasion and uncover a mechanism unique to *Cryptosporidium*. We developed a screen to identify parasite effectors, finding injection of multiple parasite proteins into the host from the rhoptry organelle. These factors are targeted to diverse locations within the host cell and its interface with the parasite. One identified effector, ROP1 accumulates in the terminal web of enterocytes through direct interaction with the host protein LMO7, an organizer of epithelial cell polarity and cell-cell adhesion. Genetic ablation of LMO7 or ROP1 in mice or parasites respectively, impacts parasite burden *in vivo* in opposite ways. Taken together, these data provide molecular insight into how *Cryptosporidium* manipulates its intestinal host niche.

## In Brief

The parasite *Cryptosporidium* infects enterocytes and causes severe diarrheal disease. Guérin *et al.* used live imaging to unravel the mechanism of parasite invasion and discover proteins secreted in this process that modify the host cell. Identifying such molecular interactions between parasite and host is key to understand and combat infection.

[†]Lead contact: Boris Striepen Tel.: 1-215-573-9167; Fax: 1-215-746-2295, striepen@upenn.edu.

Author contributions

A.G. and B.S. conceived the study. A.G. performed most experiment with contributions from N.H.R. to live microscopy and E.M.K. to the isolation of transgenic parasites. L.B. performed electron microscopy. A.G. and B.S. wrote the manuscript.

Declaration of interests

The authors declare no competing interests.

## Graphical abstract

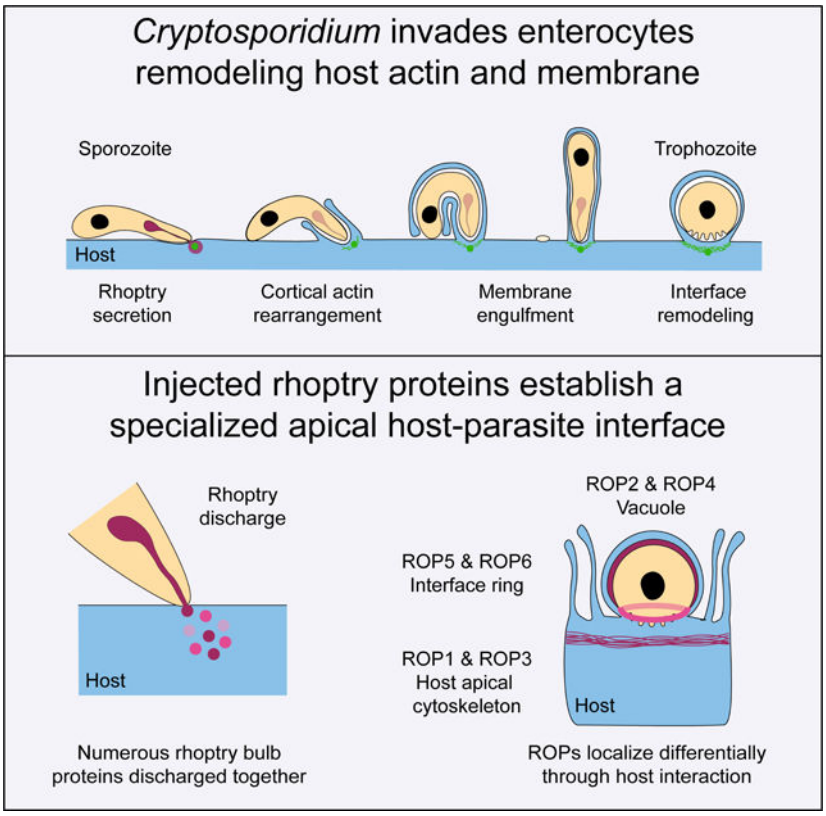


### Keywords

Cryptosporidium; Apicomplexa; invasion; rhoptry; secretion; effectors

## Introduction

The apicomplexan parasite *Cryptosporidium* is transmitted by a chlorination-resistant spore, the oocyst. This parasite is responsible for more than half of all waterborne disease outbreaks in the United States (Hlavsa et al., 2018) and is common around the world (Checkley et al., 2015). Infection causes self-limiting enteritis in immunocompetent individuals and life-threatening opportunistic infection in those suffering from primary or acquired defects in cellular immunity (Checkley et al., 2015). More recently, *Cryptosporidium* was also recognized as a leading global cause of severe diarrheal disease in young children and as an important contributor to early childhood mortality (Kotloff et al., 2013). Malnutrition renders children highly susceptible to severe and protracted cryptosporidiosis, and children in resource poor settings suffer a disproportionate burden of disease and mortality (Choy and Huston, 2020). Cryptosporidiosis in turn causes malnutrition, growth and developmental delays in children (Khalil et al., 2018).

*Cryptosporidium* primarily infects the epithelium of the intestine, where it invades enterocytes and replicates intracellularly to give rise to multiple asexual and sexual lifecycle

stages (Guerin and Striepen, 2020). The parasite resides in a peculiar parasitophorous vacuole (PV) that underlies the plasma membrane but bulges from the enterocyte into the gut lumen. *Cryptosporidium* thus develops in an intracellular but extra-cytoplasmic niche and is separated from the bulk of the host cell by multiple structures including a host actin pedestal (Elliott et al., 2001; Forney et al., 1999). Pedestal formation at the infection site depends on the host cell's Arp2/3 complex (Chen et al., 2003; Chen et al., 2004b), however, how the parasite triggers this actin polymerization event is unknown. *Cryptosporidium* invasion and host cell remodeling remains poorly understood at a mechanistic level and very few of the parasite proteins involved have been identified thus far (Lendner and Daugschies, 2014). In other apicomplexans, proteins secreted from three specialized organelles have emerged as key mediators of invasion and pathogenesis. Initially described in *Toxoplasma gondii*, micronemes have been associated with motility and invasion, rhoptries with invasion and immune modulation, and dense granules with remodeling and transcriptional subjugation of the host cell (Ben Chaabene et al., 2021; Dubremetz et al., 1998; Frenal et al., 2017; Hakimi et al., 2017). The rhoptry is of particular interest as it is capable of injecting proteins into the host cell cytoplasm and its discharge initiates invasion. Rhoptries are found at the apical end of the invasive stages and have two compartments with differentiated protein content. The apical neck contains RhOptry Neck (RON) proteins some of which anchor the parasite in the host cell during invasion, while the basal bulb portion-containing RhOPtry bulb (ROP) proteins delivers a range of pathogenesis factors to hijack the host cell (Besteiro et al., 2011; Lima and Lodoen, 2019). *Cryptosporidium* sporozoites and merozoites possess a single rhoptry (Tetley et al., 1998) but our knowledge of its function and protein content is very limited. Thus far, a single protein, CpPRP1 (cgd8_2540), a homolog of TgRON1 has been demonstrated to localize to the organelle (Valentini et al., 2012). Homologs of the secreted proteins that make up the core of the invasion mechanism of *Toxoplasma* and *Plasmodium*, the moving junction complex (AMA1/RON2/RON4/RON5), are lacking in *Cryptosporidium* which may indicate important mechanistic differences (Abrahamsen et al., 2004). Rhoptry bulb proteins are highly divergent between Apicomplexa (Kemp et al., 2013) as they are subject to host specific diversifying evolutionary pressure. Thus, rhoptry bulb proteins from other Apicomplexa offer limited guidance in deciphering the *Cryptosporidium* rhoptry proteome.

Here we used video microscopy and genetically encoded reporters to track the parasite and host cell during *Cryptosporidium* invasion. We identified potential rhoptry proteins using transcriptional profiling and validated six rhoptry bulb proteins of *Cryptosporidium* by tagging their endogenous loci. Following secretion, these proteins target diverse locations within the host cell and its interface with the parasite, suggesting a range of functions. We analyzed ROP1 (cgd3_1770) in detail and found it to be injected into the host during invasion. We identify the LIM Domain Only protein 7 (LMO7), a component of the terminal actin web of the enterocyte in mice and humans, as the host interactor targeted by ROP1. We analyze this interaction and the consequences of loss of the host and parasite factor on infection.

## Results

### *Cryptosporidium* invasion occurs through morphologically distinct phases

To gain dynamic insight into the invasion process of *Cryptosporidium*, we developed a real-time microscopy assay for *C. parvum* sporozoites. Oocysts were triggered with sodium taurodeoxycholate for 10 minutes, added to host cells prior to excystation and imaged using differential interference contrast (DIC) microscopy. After 45 minutes in this environment, sporozoites began to exit their oocyst and glide rapidly over the host cell monolayer (figure 1a), with invasion typically occurring within seconds of initial contact (video 1). For sporozoites tracked over multiple frames we measured a mean speed of 14μm/s (figure 1c, n=15 and 1b shows a representative kinogram). We recorded and analyzed more than 30 complete invasion events which allowed us to establish a sequence of stereotypic events that lead from the elongated motile sporozoite to the intracellular rounded growth stage, the trophozoite. During invasion, sporozoites curved dramatically along their longitudinal axis into a C-shape over the course of 2 minutes, parasites then relaxed into a straight form, which contracted into the rounded trophozoite over 6 additional minutes (figure 1d, 1e and video 2). Figure 1e shows the respective timing of numerous observed morphologies. Upon initiation of invasion the apical end of the sporozoite appeared spatially fixed, while the basal end showed significant relative displacement (figure 1f). We thus note that *Cryptosporidium* invasion coincides with contortion of the parasite at the surface of the host cell but does not feature penetration of the cytoplasm of the host cell or the conspicuous constriction of the moving junction observed during host cell invasion by other Apicomplexa.

### Parasitophorous vacuole formation coincides with parasite bending

We next wished to understand how the observed sequence in parasite behavior related to invasion. To observe specific compartments and molecular components simultaneously in the host and parasite, we generated reporter lines for both. First, we established a HCT8 host line in which the plasma membrane is labeled by fusing the pleckstrin homology (PH) domain of human phospholipase C to GFP (Stauffer et al., 1998). We also generated a *C. parvum* strain expressing red fluorescent TdTomato in its cytoplasm (figure S1a). Using these transgenics, we imaged invasion by fluorescence microscopy collecting dual color z-stacks every half second. As shown in video 3 and in corresponding frames in figure 2a, bending of the sporozoite coincided with the successive engulfment of the parasites by the host plasma membrane (figure S2a). Once the membrane reached the basal end, the parasite experienced an abrupt relaxation from a bent into a straight form that now was covered by membrane. This event left behind a residual dot of parasite red fluorescence on the surface of the host cell, suggesting constriction and fission at the end of internalization. The residual dot is a feature of invasion that also observed in fixed samples using a range of antibodies (figure S2b). Taken together, the parasite is fully internalized by the time it relaxes into the straight form and we conclude that *Cryptosporidium* sporozoite invasion occurs over the course of two minutes.

## Rapid polymerization of host actin occurs during *Cryptosporidium* invasion

While there is wide agreement in the literature that *Cryptosporidium* infection is associated with polymerization of host actin and pedestal formation at the invasion site, there has been debate as to whether this occurs during or following invasion (Guerin and Striepen, 2020). To address this question, we engineered a host cell transduced to express lifeact, a 17-amino acid peptide linked to green fluorescent protein, which specifically binds F-actin without disturbing cytoskeletal function (Riedl et al., 2008). We exposed these cells to TdTomato parasites and recorded parasite invasion. Video 4 shows a representative event and figure 2b selected time points. Within seconds of host-parasite contact, a spot of F-actin became visible at the apical tip of the parasite indicating actin polymerization at the earliest points of invasion. We assigned polarity based on the direction of sporozoite movement (figure 1) and confirmed assignment using Hoechst to label the basal parasite nucleus and phalloidin to detect F-actin (figure S2c). Over the internalization phase this actin structure grew more elaborate, surrounding the central spot with a wider ring. The structure showed tight association with the apex of the parasites, and was limited to that tip, importantly, we did not observe host f-actin engulfing the entire parasite. The structure was maintained throughout the intracellular development of the parasites and we used confocal as well as stimulated depletion microscopy to obtain higher resolution images (figure 2c and d). As shown in video 5 and figure 2d, host actin filaments emanate from the basal central density to the apical ring forming a cup that cradles the parasite and anchors it into the actin filaments of the terminal web. Taken together, these observations lead us to an invasion model (figure 2e) in which the parasite's apical end is fixed into the cortical cytoskeleton of the host cell and the parasite bends due to its engulfment by the host plasma membrane.

## A gene expression screen identifies *Cryptosporidium* rhoptry proteins

Our imaging studies revealed an important role of the parasite apex in its interaction with the host cytoskeleton. This is the point of secretion for micronemes and the single rhoptry. Rhoptry content is believed to be secreted during *Cryptosporidium* invasion (Chen et al., 2004a) but only a single protein has been studied thus far (Valentini et al., 2012). Using genome searches (veupathdb.org), we identified *C. parvum* homologs of the *T. gondii* rhoptry biogenesis factors Armadillo Repeats Only protein (CpARO, cgd2_370) and the palmitoyl-transferase DHHC7 (cgd1_1380) (Mueller et al., 2013; Mueller et al., 2016), as well as four putative homologs of the rhoptry neck proteins RON6 (cgd1_1870), RON9 (cgd4_2420), RON10 (cgd3_910) and RON11 (cgd3_2010) (Lamarque et al., 2012; Wang et al., 2016) but searches using rhoptry bulb proteins failed. To discover *Cryptosporidium* rhoptry proteins, we took advantage of the highly ordered apicomplexan cell cycle in which successive waves of gene expression deliver the components of various organelles (Francia and Striepen, 2014). Genes encoding rhoptry proteins are transcribed towards the end of the replication cycle when new invasive stages are assembled (figure 3a) (Behnke et al., 2010; Le Roch et al., 2003; Suarez et al., 2019). To understand when rhoptry proteins are expressed in *Cryptosporidium* we first experimentally defined the length of the lytic cycle. GFP-lifeact HCT8 cells were infected with TdTomato *C. parvum* sporozoites and subjected to live cell imaging (figure 3b, video 6). Under these conditions, *C. parvum* completes the cycle from invasion to egress in 11.5h (STD= 51.6min, figure 3c, n=29). Next, we infected coverslips and conducted a 12-hour time course experiment (figure 3d). The rhoptry neck

protein, CpPRP1, was observed only at the 10 and 12-hour time points and coincided with the presence of eight nuclei per parasite indicating the conclusion of the merogony cycle (figure 3e).

Using this information, we analyzed multiple transcriptomic datasets. First, we used RT-PCR data that measured the expression of *C. parvum* genes over the course of development in cell culture (Mauzy et al., 2012). When comparing 2, 6 and 12 hours, 400 genes showed a transcription peak at 12 hours similar to CpARO (figure 3f, CpPRP1 is absent from this dataset), and 121 of these encoded a protein with a N-terminal signal peptide. To further narrow the candidate pool, we analyzed RNAseq data from different lifecycle stages obtained from infected cultures and mice (Tandel et al., 2019). In culture, female parasites are not fertilized and thus are arrested in their development prior to sporogony and rhoptry biogenesis (Tandel et al., 2019). In contrast, *in vivo* females complete this process which is reflected in the transcription of rhoptry proteins including CpARO (figure 3g and 3h), this is also true for asexual merozoites *in vitro*. This comparison identified 163 putative rhoptry proteins. Combining both analyses yielded a final set of 54 co-transcribed candidates (figure 3i and table S1).

## Validation of six *Cryptosporidium* rhoptry bulb proteins

To test the validity of our predictions, we chose seven candidates and modified their endogenous loci using a CRISPR/Cas9 strategy (Vinayak et al., 2015) to introduce a C-terminal triple HA epitope (figure S1b). Next, we assessed the localization of these proteins by immunofluorescence assay in extracellular sporozoites and conducted time course experiments to monitor intracellular stages in culture. Tagged cgd3_1770 was observed in sporozoites, merozoites and in late asexual stages containing future merozoites recognizable by the presence of 8 nuclei (figure 4a top) but not in sexual stages which lack rhoptries. The HA staining was consistently found adjacent to CpPRP1, and in sporozoites/merozoites appeared basal to the rhoptry neck protein suggesting it localized to the bulb of the rhoptry. To test this, we fixed and froze sporozoites and sectioned samples for electron microscopy. Sections were stained with anti-HA and a secondary antibody labeled with 10 nm gold. As shown in figure 4b, gold particles heavily accumulated over the bulbus part of the rhoptry and were absent from other organelles found in close vicinity, including the micronemes and dense granules.

In further studies, five additional candidates, cgd1_950, cgd3_1710, cgd3_1730, cgd3_1780 and cgd6_3630 displayed similar localization to the rhoptry bulb (figure 4a and S3a). In cgd6_4000 tagged parasites, the fluorescence was not associated with the rhoptry (figure S3b).

## *Cryptosporidium* rhoptry proteins target different compartments of the host/parasite interface

Consistent with other apicomplexans the rhoptry of the *Cryptosporidium* sporozoite is discharged during invasion (figure S2d shows cgd3_1710 as an example). To assess the localization of rhoptry proteins following invasion, cultures were fixed for immunofluorescence assay 2 hours post infection. All six rhoptry proteins appeared to

be discharged from the organelle at that timepoint but were found in diverse locations. Two proteins, cgd3_1780 and cgd3_1730, localized exclusively to the PV highlighted by colocalization with *Vicia villosa* lectin (VVL (Gut and Nelson, 1999)), shown in green (figure 4c and S3c). These proteins have no predicted transmembrane domains, suggesting they may reside in the vacuolar space, but we lack markers and resolution to distinguish lumen and membrane. In contrast, cgd1_950 and cgd6_3630, exhibited labelling in the form of a ring at the host-parasite interface parallel to the epithelium, a structure best appreciated in side-view projections (figure 4c and S3c). Both proteins harbor a transmembrane domain at their C-termini and ankyrin repeat regions in their presumptive ectodomains. Interestingly, the last two tagged proteins, cgd3_1770 and cgd3_1710, in addition to the PV, were also found in the host cell. Cgd3_1710 appeared evenly distributed in the infected cell while cgd3_1770 accumulated at the cell periphery (figure 4c and S3c and d). We performed immunofluorescence experiments with or without permeabilization for cgd3_1770 and found the epitope accessible only after permeabilization (figure S4a) confirming its presence in the cytoplasm of the host cell. We conclude that *C. parvum* expresses numerous rhoptry bulb proteins that are targeted, and likely contribute to, a range of structures interfacing parasite and host cell. We named the proteins ROP1 (cgd3_1770), ROP2 (cgd3_1780), ROP3 (cgd3_1710), ROP4 (cgd3_1730), ROP5 (cgd1_950) and ROP6 (cgd6_3630).

## Upon injection ROP1 associates with the apical terminal web

In infected HCT8 cells, ROP1 localized to the site of infection and the cell periphery. The distribution of ROP1 was not uniform around the cell and we wondered whether this reflected cell polarity. To test this, we next infected Caco2 cells that were grown 21 days on trans-wells to establish mature junctions and apical to basolateral cell polarity (Stenberg et al., 2001). Tight junctions were visualized by staining for zonula occludens protein-1 (ZO-1). In these cells, we found parasite injected ROP1 to be apically restricted (figure 5a and video 7, in this cell type ROP3 is also apically restricted, figure S3d). We also assessed the localization of ROP1 *in vivo*. The small intestines of $ifn\gamma^{-/-}$ mice infected with ROP1-HA parasites for 7 days were processed for histology. HA staining was found only in infected cells and was restricted to the apical face of the epithelium (figure 5b left). When imaged with super-resolution microscopy, ROP1 was found to directly underlie the enterocyte brush border labeled with an antibody to villin, and to coincide with the terminal actin web (figure 5b right). Filaments previously identified as f-actin (Elliott and Clark, 2000; Elliott et al., 2001) are also visible by cryo-electron microscopy of infected HCT8 cells. Gold particle labeling ROP1 coincided with these filaments underlying the parasite at the host side of the interface (figure 5c).

Next, we expressed ROP1 directly in the host cell. The coding sequence of ROP1, omitting the signal peptide was fused to GFP and transfected into HCT8 cells by lipofection. In IFA experiments GFP was only detectable after permeabilization regardless whether fused to the N- and C-terminus (figure S4b). We found that the localization of this reporter recapitulated the localization of ROP1 injected by the parasite (figure 5d top) and that the N but not the C-terminal portion was required and sufficient for this localization (figure 5d middle and bottom). The N-terminal construct was used in subsequent experiments due to its superior expression. ROP1 accumulates in a cellular region rich in actin and we thus

wondered whether this may be due to association. To test this, we used a fractionation assay to biochemically separate fractions enriched or depleted in F-actin (Gatfield et al., 2005). GFP-N-ROP1 was found in both fractions while the negative control GFP was only found in the soluble F-actin-depleted fraction (figure 5e). Disruption of F-actin by cytochalasin D treatment disturbs ROP1 staining in transfected and infected cells (figure S4c). We conclude that ROP1, once secreted into the host cell, binds to a component of the apical terminal web in an autonomous fashion. Our experiments do not distinguish whether this is due to binding to F-actin or one of its many associated factors.

## Injected ROP1 interacts with the host protein LMO7 *in vitro* and *in vivo*

To gain insight into the host pathway targeted by ROP1 we conducted a yeast-two-hybrid (Y2H) screen to identify binding partners. The N-terminal part of ROP1 was used as bait to screen against a prey library generated from epithelial cells of the human colon. 125 million interactions were tested yielding 149 positive clones encoding 25 independents fragments of LMO7 and 7 clones represented 2 fragments of its paralog LIMCH1. All fragments contained the c-terminal LIM domain, a double zinc finger protein binding motif, shared between the two paralogs (figure 6a). Both proteins have roles in the cellular organization of the actin cytoskeleton (Du et al., 2019; Lin et al., 2017; Ooshio et al., 2004). Based on the number of clones obtained in the Y2H screen and their relative expression enterocytes (www.proteinatlas.org), we chose to focus on LMO7. We first tested the validity of the interaction between LMO7 and ROP1 by immunoprecipitation (IP). HCT8 cells transfected to express GFP-N-ROP1 or GFP were used to pull down the resulting proteins and their binding partners. When probing with an antibody to LMO7, we detected the protein in GFP-N-ROP1 but not GFP-only control samples (figure 6b). In reverse IPs performed using LMO7 antibodies bound to protein G beads, GFP-N-ROP1 but not GFP was pulled down (figure 6c). We conclude that ROP1 binds LMO7 and that based on the Y2H data this interaction is direct and mediated by the LIM domain.

LMO7 has been associated with adhesion and actin-related cell-cell contacts in epithelial cells (Ooshio et al., 2004) and the terminal actin web of hair cells in the ear (Du et al., 2019), but has not been studied in the intestine. In HCT8 cells, we found LMO7 to colocalized with ectopically expressed ROP1 (figure 6d) and during parasite infection, LMO7 accumulated at the infection site alongside actin and ROP1 (figure 6e). In uninfected mouse intestinal sections, enterocytes showed robust LMO7 labeling that was restricted to their apex and coincided with actin (figure 6f left). In *Cryptosporidium* infected mice, ROP1 and LMO7 colocalized at the apical surface of infected cells (figure 6f right).

## Mutation of LMO7 or ROP1 have opposite effects on parasite burden

To understand the functional consequence of the ROP1/LMO7 interaction, we ablated the ROP1 gene by inserting a selection marker into the coding sequence (figure S1c). This mutant provided the opportunity to test the role of ROP1 during infection. In the absence of ROP1, LMO7 was still present at the infection site in HCT8 cells *in vitro* (figure 7a), suggesting ROP1 is not necessary for LMO7 localization. The KO parasites appeared to grow at a comparable rate to WT parasites in cell culture, and we thus conclude that ROP1 is not required for parasite invasion and growth *in vitro* (figure 7b and S5a). Next, we

investigated the role of LMO7 in infection. Mice in which LMO7 is disrupted were recently generated to study its role in auditory hair cells (Du et al., 2019). LMO7 is subject to complex differential and tissue specific splicing (Friedberg, 2009) we thus demonstrated that LMO7 its loss from the intestine of these KO mice (figure S5b). Immunocompetent mice are resistant to infection with *C. parvum*. To infect LMO7 KO mice, we neutralized interferon γ by antibody treatment (Griffiths et al., 1998; Sateriale et al., 2019) and processed the intestines of infected animals for immunofluorescence assays. In LMO7 KO mice, accumulation of parasite injected ROP1 within the terminal web was lost (figure 7c). We conclude that LMO7 recruits ROP1 to its site of action and that the localization of LMO7 at the site of infection is independent of ROP1. Next, we evaluated the relative impact of the loss of LMO7 and ROP1 on parasite burden *in vivo*. When scoring parasite burden by fecal luciferase activity, we observed increased parasite shedding in LMO7 KO mice when compared to C57BL6 wild type. Figure 7d shows 15-fold higher activity (area under the curve) and is a representative example of three biological repeats. In contrast, when comparing parasite shedding between the ROP1 KO parasite with a control strain in which the locus was tagged but not disrupted, we found luciferase activity reduced by 8.7-fold (figure 7e). Overall, these results are consistent with a model in which LMO7 is participating in a host protective process and ROP1 is acting as a rhoptry effector with impact on parasite burden *in vivo*.

## Discussion

Apicomplexan parasites have evolved highly specialized pathogenesis factors allowing them to invade and take control of a diverse range of host cells. Electron microscopy shows dramatic remodeling of epithelial cells during *Cryptosporidium* infection but the mechanisms behind these changes remain unknown. Our efforts to observe *Cryptosporidium* sporozoite invasion in real time revealed parallels with related parasites but also crucial differences. Like the infectious stages of other apicomplexans, *C. parvum* sporozoites move by gliding and they do so at a remarkable speed (14μm/s compared to 1–2 for *Plasmodium* sporozoites and *T. gondii* sporozoites and tachyzoites (Hakansson et al., 1999)(Wetzel et al., 2005)(Amino et al., 2006). We measure slightly higher speeds than previous authors for *C. parvum* (Wetzel et al., 2005), a difference that may result from the use of cells versus coated coverslips. Whereas other apicomplexans translocate fully into their host cells (Besteiro et al., 2011), our DIC and fluorescence-based imaging instead documents that the *C. parvum* sporozoite never enters the bulk of the cell. Furthermore, we do not observe the constriction associated with the moving junction, this finding is consistent with the absence of the genes for proteins that build this structure, in particular the conserved apical membrane antigen 1 and rhoptry neck protein 2 (Tonkin et al., 2011), from the *C. parvum* genome (Abrahamsen et al., 2004). Some of our observations match the capped junction model described as a special case of *T. gondii* invasion, where the host membrane is pulled around a parasite that remains spatially fixed due to the stiffness of the host cortex (Bichet et al., 2014). *Cryptosporidium* exclusively invades epithelial cells with a robust cortical skeleton and further stimulates actin polymerization (Elliott et al., 2001). Actin modification initiates immediately with apical contact and locks the parasite into the terminal web (figure 2). This structure maintains its position at the host membrane, and we do not observe host

actin fully engulfing the parasite. Using cytochalasin D treatment, parasite F-actin has been shown to be required for invasion (Wetzel et al., 2005). Completion of invasion resulted in observable fission. How this fission occurs is unknown but it may indicate the presence of a junction-like structure of undefined composition.

Previous studies suggested surface contact mediated engagement of host integrin signaling as a trigger for actin polymerization (Zhang et al., 2012), alternatively, or in addition, injected factors could act in this fashion as observed for many bacterial pathogens (Kenny et al., 1997; Ribet and Cossart, 2015). Here we report the discovery of six *C. parvum* rhoptry bulb proteins and find them to target a variety of locations. ROP2 and 4 are part of the parasitophorous vacuole while the localizations of ROP5 and its paralog ROP6 make them prime candidates for parasite components of the ring-shaped tight junction that constrains the host parasite interface (Guerin and Striepen, 2020; Ostrovska and Paperna, 1990). Two of the six rhoptry factors, ROP1 and 3, were injected into the host cell and ROP1 caught our particular interest for its association with the apical cytoskeleton of the enterocyte. This association is mediated by physical binding of the N-terminus of ROP1 to the c-terminal LIM domain of LMO7 and this interaction is rigorously supported by Y2H assay, co-immunoprecipitation, and cellular colocalization *in vitro* and *in vivo*. Lastly, loss of LMO7 resulted in loss of apical accumulation of ROP1, further validating their association and indicating that it is the host protein that recruits the parasite factor.

LMO7 is a cytoskeletal modulator that has been associated with the condensation of F-actin at cell junctions and in the terminal web of epithelia and sensory cells (Du et al., 2019). LMO7 directly binds to afadin and alpha-actinin connecting the nectin/afadin and E-cadherin/catenin complexes at the adherens junctions (Ooshio et al., 2004). Numerous studies have tied the protein to the relative invasiveness of tumors (Furuya et al., 2002; Kang et al., 2000; Nakamura et al., 2005; Sasaki et al., 2003) further supporting its role in epithelial cohesion. Its *Drosophila* homolog Smash, which similarly accumulates at adherens junctions, regulates planar cell polarity and actomyosin-dependent apical constriction of epithelial cells (Beati et al., 2018). Both mouse and fly protein have also been shown to impact epithelial cell death and proliferation through apoptosis (Liu et al., 2021; Tanaka et al., 2019). Interestingly, flies in which this gene was mutated showed enhanced susceptibility to infection (Lu et al., 2015).

A wide array of pathogens evolved effectors to hijack host actin interfering at essentially every step of the actin regulatory cascade. These effectors can target actin directly, or a range of associated proteins and aid attachment, invasion and spread, or interfere with cellular defenses that require motility or vesicular trafficking including phagocytosis and autophagy (Colonne et al., 2016). Actin can be directly involved in pathogen restriction through inflammasome triggered cell extrusion as shown for *Salmonella* (Rauch et al., 2017). Actin dynamics are also crucial to epithelial cell junctions which is particularly relevant to the dissemination of entero-pathogens and the development of diarrheal symptoms (Guttman and Finlay, 2009). Enteropathogenic *Escherichia coli* (EPEC) injects multiple effectors to induce actin rearrangement, dephosphorylation of Occludin, disruption of the microtubule network, and inhibition of tight junction protein synthesis which collectively contributes to tight junction disruption (reviewed in (Ugalde-Silva et al., 2016)). We were thus interested

to assess whether LMO7 involvement is restricted to *Cryptosporidium*. Experiments with EPEC and HCT8 cells showed recruitment of LMO7 to the actin pedestal induced by these bacteria (figure 7f) similar to that observed for other junctional proteins (Hanajima-Ozawa et al., 2007). This may suggest a broader role for LMO7 during infection with entero-pathogens.

In the context of *Cryptosporidium* infection, *in vitro* invasion and pedestal formation appear normal in the absence of ROP1 arguing against a direct role in this process. Our *in vivo* experiments show enhanced susceptibility in the absence of LMO7. Further work is required to understand the significance of this result. Epithelial cohesion and homeostasis are perturbed by *Cryptosporidium* infection. Infection is associated with cholera-like diarrhea and has been shown to destabilize tight and adherens junctions *in vitro* and *in vivo* (Griffiths et al., 1994; Kumar et al., 2018) and to induce enhanced epithelial cell turnover *in vivo* (Sateriale et al., 2019). *Cryptosporidium* also potently triggers a host cell intrinsic inflammasome (McNair et al., 2018; Sateriale et al., 2021) and this may result in host cell death and extrusion (Ojcius et al., 1999). ROP1 binds the LIM domain of LMO7, a domain that is essential to the function of both LMO7 and Smash (Beati et al., 2018; Du et al., 2019). ROP1 thus may disrupt LMO7 dependent processes by blocking its interaction with its natural partner(s).

Our screen identified a long list of candidate pathogenesis factors beyond ROP1, unraveling their targets and function will likely lead to a deeper understanding of how this important parasite invades and hijacks cells to evade the defenses of its host.

## STAR Methods

### RESOURCE AVAILABILITY

**Lead contact—**For access to reagents or parasite strains used in this study please contact the Lead Contact, Boris Striepen (striepen@upenn.edu).

**Material availability—**All unique/stable reagents generated in this study are available from the Lead Contact.

**Data and code availability—**All data reported in this paper will be shared by the lead contact upon request. This paper does not report original code. Any additional information required to reanalyze the data reported in this paper is available from the lead contact upon request.

### EXPERIMENTAL MODEL AND SUBJECT DETAILS

**Mouse Models of Infection—**C57BL/6 (stock no:000664) and *ifnγ* $^{-/-}$ (stock no:002287) were purchased from Jackson Laboratory. LMO7 KO mice were obtained by Dr. Jung-Bum Shin and bred in house (Du et al., 2019). All mice were gender and age matched within individual experiments (ranging from 6 to 8 weeks). Both males and females were used and no differences were observed. All protocols for animal experimentation were approved by the Institutional Animal Care and Use Committee of the University of Pennsylvania (protocol #806292).

**Parasite Strains—***Cryptosporidium parvum* oocysts were purchased from Bunchgrass Farms. Transgenic strains were propagated within infected *ifnγ* $^{-/-}$ mice (stock no:002287 bred in house). Oocysts were then purified from fecal collections using sucrose flotation followed by a cesium chloride gradient (see Method Details).

**Host cell culture—**HCT8, HEK293 and Caco2 cells, obtained from ATCC, were cultured in DMEM supplemented with 10% FBS at 37C with 5% CO2. For differentiation, $1.10^5$ Caco2 cells were seeded onto trans-well dishes (6,5mm diameter; pore size 0.4μm; Costar) and grown for 21 days with media changed every other day.

## METHOD DETAILS

**Plasmid construction—**A human-optimized recodonized fragment of ROP1 without its signal peptide was generated by Integrated DNA Technologies (IDT). The fragment was TOPO cloned, sequenced and amplified using primers AG257/AG258 while the vector CMV-GFP was amplified using the primers AG255/AG256 (Table S2). Both fragments were cloned by Gibson Assembly and the final vector CMV-GFP-ROP1 FL was sequenced. For the generation of GFP-ROP1 N-terminal (73–793nt) and C-terminal (794–1583nt), both vectors were generated by Gibson Assembly with respectively primers AG297/AG298 and AG319/AG320 from the CMV-GFP-ROP1 FL vector. To generate CMV-ROP1-FL-GFP, ROP1 was amplified from the TOPO vector using AG203/AG204 while the vector CMV-GFP was amplified using the primers AG205/AG206.

**Generation of stable transgenic HCT8—**The GFP-PLCdelta-PH fragment was amplified from addgene vector #21179 using primer AG64 and AG65 and inserted into pDONR221 plasmid using Gateway LR clonase prior to recombination with the destination vector PLX301. Similarly, GFP-lifeact fragment was amplified from the GFP-lifeact vector obtained from Dr. R. Wedlich-Soeldner (Max Planck Institute of Biochemistry, Martinsreid Germany). Lentivirus was produced in $75cm^2$ flasks of HEK293 cells by co-lipofection of vectors PLX301-GFP-PLC, VSVg and PAX2 as previously described (Yang et al., 2011). After 48 hours, the supernatant was collected and centrifuged 5 minutes at 2500rpm, filtered through 0.45μm and centrifuge for 15,5 hours at 4C 15,000g. The pellet was resuspended in 1ml of DMEM + 10% FBS + 1% BSA.

HCT8 cells were plated onto P24 well dishes to reach 50–60% confluency. Polybrene was added to the cells at a final concentration of 1μg/ml as well as 100μl of either GFP-lifeact or GFP-PLC lentivirus suspension. Cells were centrifuged at 1000g for 2 hours at 30C before being incubated 30 minutes at 37C. The media was replaced, cells were incubated overnight at 37C, and after 48 hours, cells were selected with 1.5μM of puromycin, followed by cloning through serial dilution. Clones were assessed for the expression of GFP by microscopy.

**Transient transfection of HCT8—**HCT8 cells were transiently transfected with GFP and different GFP-ROP1 fusion constructs using lipofectamine 3000. Briefly, cells were seeded onto coverslips or flask to reach 70% confluency on the day of transfection. For coverslips, 500ng vector was incubated for 20 minutes at RT in 50μl of optiMEM with 1μl

lipofectamine 3000 and 2µl of lipofectamine 3000 reagent. For flaks volumes were scale proportionally. The cells were washed 3 times with optiMEM prior to incubation with the DNA/lipofectamine mixture for 4 hours at 37C, washed again and changed to regular media and fixed or lysed the following day.

**Generation of transgenic parasites—**Transgenic parasites were generated as previously described (Sateriale et al., 2020; Tandel et al., 2019). Briefly, for C-terminal tagging, a guide RNA targeting the 3'UTR of the gene of interest was cloned into the Cas9/gRNA plasmid. A repair fragment was PCR amplified from plasmid pLic-3HA-Nluc-Neo with specific primers for the gene of interest and 30bp of homology arms to trigger integration. Oocysts were excysted and sporozoites were electroporated with an Amaxa 4D device (Lonza), used to infect mice by gavage (*ifnγ* $^{-/-}$, bred in-house), and transgenics were selected with paromomycin provided in the drinking water. Feces were collected, oocysts were purified, and 5' and 3' integration of the cassette was confirmed by PCR for each transgenic strain. Note that the first candidate cgd3_1770 was chosen randomly; cgd3_1780 was chosen as a cgd3_1770 paralog; cgd3_1710 and cgd3_1730 were chosen as part of the same chromosome 3 region, which we thought may represent a pathogenicity island; cgd1_950 and its paralog cgd6_3630 were chosen for their ankyrin domain and the presence of a transmembrane domain.

Cgd3_1770-HA (Guide AG67/68_Amplification AG69/70_Integration AG103/104)

Cgd3_1780-HA (Guide AG195/196_Amplification AG197/198_Integration 225/226)

Cgd3_1730-HA (Guide 335/336_Amplification AG337/338_Integration AG339/340)

Cgd3_1710-HA (Guide AG239/240 _Amplification AG241/242_Integration AG243/244)

Cgd6_4000-HA (Guide AG122/123 _Amplification AG124/125_Integration AG163/164)

Cgd1_950-HA (Guide AG233/234 _Amplification AG235/236_Integration AG237/238)

Cgd6_3630-HA (Guide AG439/440 _Amplification AG247/441_Integration AG249/442)

For the generation of the red fluorescent strain, a guide targeting the TK locus previously published (Tandel et al., 2019) was used to insert the Nluc-neo-2A-TdTomato fragment amplified with primers AG160/8522. This allows the expression of TdTomato protein in the parasite cytoplasm of all stages.

The ROP1 gene was disrupted by inserting the Nluc-neo cassette at the beginning of the coding sequence (Guide AG341/342_Amplification AG343/344_Integratoin AG260/361). KO was validated by measuring transcript after 22-hour invasion in HCT8. RNA was extracted using the RNeasy Plus mini kit and cDNA was generated using the SuperScript IV First-Strand Synthesis System. Primers AG457/458 were used to detect ROP1 transcript while 18S primers were used as a cDNA control. All the integration PCR can be found in figure S1.

**Video microscopy invasion—**HCT8 cells were grow in 8 well microslides to 70% confluency. 1 million oocysts, WT or expressing TdTomato, were excysted as previously described using the bile salt sodium taurodeoxycholate (Vinayak et al., 2015) prior to addition to slide which were mounted to microscope and kept at 37C (sporozoites emerge 45 minutes into incubation). We determined that free sporozoites rapidly deteriorate in preliminary experimentation and therefore directly added the unexcysted but triggered oocysts onto the cell monolayer. DIC images were recorded every 500ms on a Zeiss Axiovert 200 M inverted microscope equipped with an MS-2000 automatic stage (Applied Scientific Instruments) and an environmental chamber using Slidebook 6.0 software (Intelligent Imaging Innovation). For GFP-lifeact and GFP-PLC cells 4μm fluorescence image z-stacks were recorded on an OMX SR Delta Vision with automatic stage and environmental chamber. To minimize bleaching, the recording was manually activated when extracellular parasites were observed in the field of view. Videos were analyzed with Volocity and ImageJ softwares.

**Video microscopy replication—**8 chamber microslides seeded with HCT8 cell expressing GFP-lifeact were infected with 200.000 oocysts of TdTomato parasites and imaged with a delta vision OMX SR Delta Vision or a Leica DMI4000 spinning disk microscope at 5% CO2 level and 37C. Red and green channel on 6μm z-sections were recorded for 14 to 24h every 10 or 15 minutes on both instruments. No phototoxicity was observed under these conditions and 29 events showing a full invasion to egress cycle were observed.

**Immunofluorescence microscopy—**P24 well HCT8 coverslip cultures were infected with triggered oocyst and incubated 1h to observe invasion, 3h for trophozoites and sporozoites, and 24h for meronts. Cells were fixed with cold methanol for 7 minutes at −20C to visualize proteins inside the rhoptry organelle or with 4% paraformaldehyde for 30 minutes at room temperature for other locations. Cells were treated with 1μM cytochalasin D 2h after invasion (or 24h after HCT8 transfection) for 30 minutes prior to fixation with 4% paraformaldehyde. Immunofluorescence was performed as described (Tandel et al., 2019). Briefly after permeabilization with 0.5% Triton x100 for 15 minutes, the cells were incubated for 1 h with 4% FBS, followed by primary antibodies in 1% FBS for 1h (see STAR table), washes in PBS, and secondary antibodies in 1% FBS for 1h. Finally, after 5 minutes incubation with Hoechst, cells were washed 3 time in PBS and mounted on slides using Vectashield and sealed with nail polish. For permeabilization assays, the triton x100 step was omitted.

Intestines of infected mice were harvested and ‘swiss-rolled’ prior to fixation overnight in formalin (Sateriale et al., 2020). Note that to visualize LMO7 in the intestine, 30 min fixation with 4% PFA was required. Samples were incubated in 30% sucrose overnight before mounting in OCT. Cryo-sectioning was performed by the PennVet Pathology core facility and immunofluorescence was performed as described (Sateriale et al., 2020).

For EPEC infection of HCT8, bacteria were grown overnight at 37C in LB before being incubating 3h at 37C in DMEM without antibiotics as previously described (Hanajima-Ozawa et al., 2007). The bacteria were then incubated on HCT8 coverslips for 1 hour at a

MOI of 20. The unattached bacteria were washed out with PBS prior to fixation with 4% paraformaldehyde. Actin and Hoechst were used to localize the attached bacteria.

Samples were imaged using a widefield Leica DM6000B, an OMX SR Delta Vision, a Leica DMI 6000B confocal microscope or a Leica SP8 HyVolution 2 Confocal SuperResolution system.

**Immunoelectron microscopy—**For immunoelectron microscopy excysted sporozoites were fixed in 4% paraformaldehyde for 30 minutes at RT, kept in fixative at 4°C until incubation in 0.1% glycine in phosphate buffer, pelleted and embedded in 12% gelatine (porcine skin gelatine, Sigma). Gelatine blocks were cut into cubes (< 1mm) and infused 24 hours in 2.3M sucrose on a rotating wheel at 4°C. Cubes were mounted onto specimen pins and frozen in liquid nitrogen. Sectioning was performed on a Leica UC7 cryo-ultramicrotome, 80 nm cryosections were picked-up in a 1:1 mixture of 2.3M sucrose and 2% methylcellulose in water, laid on nickel grids and stored at 4°C. For on-grid immunodetection, grids were floated on PBS 2% gelatine 30 minutes at 37°C to remove methylcellulose/sucrose mixture, then blocked with 1% skin-fish gelatine in PBS for 5 minutes. Successive incubation steps were performed on consecutive drops of rat monoclonal anti-HA (clone 3F10, Roche) in 1% BSA, rabbit polyclonal anti-rat IgG antibody (Sigma) in PBS 1% BSA, Protein A-gold (UMC Utrecht) in PBS 1% BSA. Four 2 minutes washes in PBS 0.1% BSA were performed between steps. After Protein A, grids were washed 4 times 2 minutes with PBS, fixed 5minutes in 1% glutaraldehyde in water then washed 6 times 2 minutes with distilled water. Grids were then incubated with 2% methylcellulose: 4% uranyl acetate 9:1 15 minutes on ice in the dark, picked-up on a wire loop and air-dried. Observation and image acquisition was performed on a Jeol 1200 EXII transmission electron microscope at the Electron Microscopy Platform of the University of Montpellier.

**Yeast-two-hybrid screen—**Y2H screening was performed by Hybrigenics Services SAS as previously described (Guerin et al., 2017). Briefly, the bait construct was a fragment of the ROP1 gene, corresponding to AA 25 to 267, cloned into pB27 as an N-terminal fusion (LexA-ROP1). The construct was used as bait to screen a colon tumor epithelial cells cDNA library (a mix of Caco2, HCA7, Colo205, SW480 cells). Note that the dominant LMO7 transcript in HCT8 is LMO7–218, a splicing variant containing PDZ and LIM domains but lacking the Calponin Homology domain.

**Immunoprecipitation—**Immunoprecipitations were performed on transiently transfected HCT8 cultures and one 75cm$^2$ flask was used for each condition. GFP-trap beads were used following the manufacturer's protocol (chromotek). Briefly, cells were washed with PBS, scraped and incubated with 500µl of Pierce buffer (ThermoFisher 87787) with protease inhibitor for 30 minutes on ice prior to sonication. The lysate was cleared at 20.000g for 10 minutes at 4C and diluted with 500µl of wash buffer (50mM Tris/ 150mM NaCl/ 0.5mM EDTA/ 0,02% Tween20/ protease inhibitor). The lysate was used as input on 50µl of beads and rotated at 4C for 1h. The flow through was recovered and the magnetic beads were washed 3 times with wash buffer. Elution was performed using 100µl of 2x SDS-loading buffer containing DTT and boiling for 10 minutes. For LMO7 IP, 2µg of mouse LMO7

antibody was covalently linked to 50µl of protein G beads using BS3 conjugation buffer following manufacturer's protocol. The IP was performed as described above but PBS with 0.02% Tween was used as wash. The input, flow through, second wash and elution fractions were run on an SDS gel and Western blot was performed using rabbit anti-GFP antibody diluted 1/2000 and anti-LMO7 mouse antibody diluted 1/250 and secondary anti-rabbit IRDye 800 and anti-mouse IRDye 680. Blots were imaged using an Odyssey Licor device.

**Actin fractionation—**Transfected cells were resuspended with cold cytoskeletal stabilizing lysis buffer (Gatfield et al., 2005) for 5 minutes on ice (80mM PIPES pH 6.9/ 1% Triton X-100/ 10% Glycerol/ 1mM EGTA/ 2.5mM MgCl2/ 1mM Na3 VO4/ 5mM NaF/ protease inhibitor). After centrifugation for 5 minutes at 5,000g 4C, the supernatant was transferred into a fresh tube and labelled F-actin depleted fraction. The pellet was then resuspended in NARC buffer (20mM HEPEX pH 7.9/ 400mM NaCl/ 1mM EDTA/ 1mM Na3 VO4/ 5mM NaF/ protease inhibitor) and vortexed for 1h, 4C prior to 10 minutes centrifugation at 16,000 g, 4C. This supernatant corresponds to the F-actin enriched fraction.

**P96 well plate growth assay—**A 96 well plate growth assay was performed by incubating 10,000 excysted oocysts of ROP1-HA or ROP1 KO strain per well of HCT8 in triplicate for 24 hours. After a wash in PBS, cells were lysed in 50µl of Nluc buffer and nanoluciferase was measured (Vinayak et al., 2015). 3 independent biological experiments were performed each in technical triplicate.

**Animal infections—**To passage transgenic parasites, *ifnγ* $^{-/-}$ mice were infected with 10,000 oocysts and paromomycin was given in the drinking water. To compare parasite virulence between ROP1-HA and ROP1 KO, age and sex matched *ifnγ* $^{-/-}$ mice were infected with 6,000 oocysts matched by number of passage and purification date. 3 mice per cage and a total of 3 cages per group were used and burden was measured by nanoluciferase assay of feces. Area under the curve was decreased with the KO by 7.2, 24 and 8.7 for each experiment corresponding to an average of 13.3 time lower with the ROP1 KO parasite. One representative experiment comparing two cages of 3 mice is in figure 7e (area under the curve 8.7).

Age and sex matched LMO7 KO (obtained from (Du et al., 2019) and bred in house) and C57BL/6 wild type mice were infected with 5,000 oocysts of the same batch. Mice were injected intraperitoneally with 1µg of IFN-gamma blocking antibodies at day −2, day 2 and day 8 post infection. A total of 10 mice per group in 3 independent experiments was used. Area under the curve was increased in the KO mice by 15.2, 18.3 and 15.3 for each experiment corresponding to an average of 16.25 time higher in the LMO7 KO mice. One representative experiment comparing two cages of 4 mice is in figure 7d (area under the curve 15.3).

## QUANTIFICATION AND STATISTICAL ANALYSIS

GraphPad PRISM was used for statistical analyses and standard deviation is displayed on graphs. A standard T-test was used to measure the difference between two populations. No statistical tests were used to predetermine sample size and no animals were excluded from

results. Figure 7c is a technical triplicate with N=3; figure 7d, N=3 with a total of 10 mice per group; figure 7e, N=3 with a total of 9 mice per group.

## KEY RESOURCES TABLE

## Supplementary Material

Refer to Web version on PubMed Central for supplementary material.

## Acknowledgments

We thank Dieter Schifferli who provided EPEC and Maryse Lebrun and Christopher Hunter for reading of the manuscript. This work was funded in part by grants from the National Institutes of Health (R01AI112427 & R01AI148249) and the Pennsylvania Department of Health to B.S., and an EMBO postdoctoral fellowship to A.G. (ALTF 58–2018).

## References

Abrahamsen MS, Templeton TJ, Enomoto S, Abrahante JE, Zhu G, Lancto CA, Deng M, Liu C, Widmer G, Tzipori S, et al. (2004). Complete genome sequence of the apicomplexan, Cryptosporidium parvum. Science 304, 441–445. [PubMed: 15044751]

Amino R, Thiberge S, Martin B, Celli S, Shorte S, Frischknecht F, and Menard R. (2006). Quantitative imaging of Plasmodium transmission from mosquito to mammal. Nat Med12, 220–224. [PubMed: 16429144]

Beati H, Peek I, Hordowska P, Honemann-Capito M, Glashauser J, Renschler FA, Kakanj P, Ramrath A, Leptin M, Luschnig S, et al. (2018). The adherens junction-associated LIM domain protein Smallish regulates epithelial morphogenesis. J Cell Biol 217, 1079–1095. [PubMed: 29358210]

Behnke MS, Wootton JC, Lehmann MM, Radke JB, Lucas O, Nawas J, Sibley LD, and White MW (2010). Coordinated Progression through Two Subtranscriptomes Underlies the Tachyzoite Cycle of Toxoplasma gondii. Plos One 5.

Ben Chaabene R, Lentini G, and Soldati-Favre D. (2021). Biogenesis and discharge of the rhoptries: Key organelles for entry and hijack of host cells by the Apicomplexa. Mol Microbiol115, 453–465. [PubMed: 33368727]

Besteiro S, Dubremetz JF, and Lebrun M. (2011). The moving junction of apicomplexan parasites: a key structure for invasion. Cell Microbiol13, 797–805. [PubMed: 21535344]

Bichet M, Joly C, Henni AH, Guilbert T, Xemard M, Tafani V, Lagal V, Charras G, and Tardieux I. (2014). The toxoplasma-host cell junction is anchored to the cell cortex to sustain parasite invasive force. BMC Biol12, 773. [PubMed: 25551479]

Checkley W, White AC Jr., Jaganath D, Arrowood MJ, Chalmers RM, Chen XM, Fayer R, Griffiths JK, Guerrant RL, Hedstrom L, et al. (2015). A review of the global burden, novel diagnostics, therapeutics, and vaccine targets for cryptosporidium. Lancet Infect Dis 15, 85–94. [PubMed: 25278220]

Chen X, Ohara SP, Huang BQ, Nelson JB, Lin J, Zhu G, Ward HD, and LaRusso NF (2004a). Apical organelle discharge by Cryptosporidium parvum is temperature-, cytoskeleton- and intracellular calcium-dependent and required for host cell invasion. Molecular Biology of the Cell 15, 466a–467a.

Chen XM, Huang BQ, Splinter PL, Cao H, Zhu G, McNiven MA, and LaRusso NF (2003). Cryptosporidium parvum invasion of biliary epithelia requires host cell tyrosine phosphorylation of cortactin via c-Src. Gastroenterology 125, 216–228. [PubMed: 12851885]

Chen XM, Huang BQ, Splinter PL, Orth JD, Billadeau DD, McNiven MA, and LaRusso NF (2004b). Cdc42 and the actin-related protein/neural Wiskott-Aldrich syndrome protein network mediate cellular invasion by Cryptosporidium parvum. Infect Immun 72, 3011–3021. [PubMed: 15102814]

Choy RKM, and Huston CD (2020). Cryptosporidiosis should be designated as a tropical disease by the US Food and Drug Administration. PloS neglected tropical diseases in press.

Colonne PM, Winchell CG, and Voth DE (2016). Hijacking Host Cell Highways: Manipulation of the Host Actin Cytoskeleton by Obligate Intracellular Bacterial Pathogens. Front Cell Infect Microbiol 6, 107. [PubMed: 27713866]

Du TT, Dewey JB, Wagner EL, Cui R, Heo J, Park JJ, Francis SP, Perez-Reyes E, Guillot SJ, Sherman NE, et al. (2019). LMO7 deficiency reveals the significance of the cuticular plate for hearing function. Nat Commun 10, 1117. [PubMed: 30850599]

Dubremetz JF, Garcia-Reguet N, Conseil V, and Fourmaux MN (1998). Apical organelles and host-cell invasion by Apicomplexa. Int J Parasitol 28, 1007–1013. [PubMed: 9724870]

Elliott DA, and Clark DP (2000). Cryptosporidium parvum induces host cell actin accumulation at the host-parasite interface. Infect Immun 68, 2315–2322. [PubMed: 10722635]

Elliott DA, Coleman DJ, Lane MA, May RC, Machesky LM, and Clark DP (2001). Cryptosporidium parvum infection requires host cell actin polymerization. Infect Immun 69, 5940–5942. [PubMed: 11500478]

Forney JR, DeWald DB, Yang S, Speer CA, and Healey MC (1999). A role for host phosphoinositide 3-kinase and cytoskeletal remodeling during Cryptosporidium parvum infection. Infect Immun 67, 844–852. [PubMed: 9916099]

Francia ME, and Striepen B. (2014). Cell division in apicomplexan parasites. Nat Rev Microbiol12, 125–136. [PubMed: 24384598]

Frenal K, Dubremetz JF, Lebrun M, and Soldati-Favre D. (2017). Gliding motility powers invasion and egress in Apicomplexa. Nat Rev Microbiol15, 645–660. [PubMed: 28867819]

Friedberg F. (2009). Alternative splicing for members of human mosaic domain superfamilies. I. The CH and LIM domains containing group of proteins. Mol Biol Rep36, 1059–1081. [PubMed: 18553215]

Furuya M, Tsuji N, Endoh T, Moriai R, Kobayashi D, Yagihashi A, and Watanabe N. (2002). A novel gene containing PDZ and LIM domains, PCD1, is overexpressed in human colorectal cancer. Anticancer Res22, 4183–4186. [PubMed: 12553053]

Gatfield J, Albrecht I, Zanolari B, Steinmetz MO, and Pieters J. (2005). Association of the leukocyte plasma membrane with the actin cytoskeleton through coiled coil-mediated trimeric coronin 1 molecules. Mol Biol Cell16, 2786–2798. [PubMed: 15800061]

Griffiths JK, Moore R, Dooley S, Keusch GT, and Tzipori S. (1994). Cryptosporidium parvum infection of Caco-2 cell monolayers induces an apical monolayer defect, selectively increases transmonolayer permeability, and causes epithelial cell death. Infect Immun62, 4506–4514. [PubMed: 7927716]

Griffiths JK, Theodos C, Paris M, and Tzipori S. (1998). The gamma interferon gene knockout mouse: a highly sensitive model for evaluation of therapeutic agents against Cryptosporidium parvum. J Clin Microbiol36, 2503–2508. [PubMed: 9705383]

Guerin A, Corrales RM, Parker ML, Lamarque MH, Jacot D, El Hajj H, Soldati-Favre D, Boulanger MJ, and Lebrun M. (2017). Efficient invasion by Toxoplasma depends on the subversion of host protein networks. Nat Microbiol2, 1358–1366. [PubMed: 28848228]

Guerin A, and Striepen B. (2020). The Biology of the Intestinal Intracellular Parasite Cryptosporidium. Cell Host Microbe28, 509–515. [PubMed: 33031769]

Gut J, and Nelson RG (1999). Cryptosporidium parvum: synchronized excystation in vitro and evaluation of sporozoite infectivity with a new lectin-based assay. J Eukaryot Microbiol 46, 56S–57S. [PubMed: 10519247]

Guttman JA, and Finlay BB (2009). Tight junctions as targets of infectious agents. Biochim Biophys Acta 1788, 832–841. [PubMed: 19059200]

Hakansson S, Morisaki H, Heuser J, and Sibley LD (1999). Time-lapse video microscopy of gliding motility in Toxoplasma gondii reveals a novel, biphasic mechanism of cell locomotion. Mol Biol Cell 10, 3539–3547. [PubMed: 10564254]

Hakimi MA, Olias P, and Sibley LD (2017). Toxoplasma Effectors Targeting Host Signaling and Transcription. Clin Microbiol Rev 30, 615–645. [PubMed: 28404792]

Hanajima-Ozawa M, Matsuzawa T, Fukui A, Kamitani S, Ohnishi H, Abe A, Horiguchi Y, and Miyake M. (2007). Enteropathogenic Escherichia coli, Shigella flexneri, and Listeria monocytogenes

recruit a junctional protein, zonula occludens-1, to actin tails and pedestals. Infect Immun75, 565–573. [PubMed: 17118974]

Hlavsa MC, Cikesh BL, Roberts VA, Kahler AM, Vigar M, Hilborn ED, Wade TJ, Roellig DM, Murphy JL, Xiao LH, et al. (2018). Outbreaks associated with treated recreational water - United States, 2000–2014 (Reprinted from Am J Transplant vol 67, pg 547–551, 2018). Am J Transplant 18, 1815–1819.

Kang S, Xu H, Duan X, Liu JJ, He Z, Yu F, Zhou S, Meng XQ, Cao M, and Kennedy GC (2000). PCD1, a novel gene containing PDZ and LIM domains, is overexpressed in several human cancers. Cancer Res 60, 5296–5302. [PubMed: 11016661]

Kemp LE, Yamamoto M, and Soldati-Favre D. (2013). Subversion of host cellular functions by the apicomplexan parasites. Fems Microbiology Reviews37, 607–631. [PubMed: 23186105]

Kenny B, DeVinney R, Stein M, Reinscheid DJ, Frey EA, and Finlay BB (1997). Enteropathogenic E. coli (EPEC) transfers its receptor for intimate adherence into mammalian cells. Cell 91, 511–520. [PubMed: 9390560]

Khalil IA, Troeger C, Rao PC, Blacker BF, Brown A, Brewer TG, Colombara DV, De Hostos EL, Engmann C, Guerrant RL, et al. (2018). Morbidity, mortality, and long-term consequences associated with diarrhoea from Cryptosporidium infection in children younger than 5 years: a meta-analyses study. Lancet Glob Health 6, e758–e768. [PubMed: 29903377]

Kotloff KL, Nataro JP, Blackwelder WC, Nasrin D, Farag TH, Panchalingam S, Wu Y, Sow SO, Sur D, Breiman RF, et al. (2013). Burden and aetiology of diarrhoeal disease in infants and young children in developing countries (the Global Enteric Multicenter Study, GEMS): a prospective, case-control study. Lancet 382, 209–222. [PubMed: 23680352]

Kumar A, Chatterjee I, Anbazhagan AN, Jayawardena D, Priyamvada S, Alrefai WA, Sun J, Borthakur A, and Dudeja PK (2018). Cryptosporidium parvum disrupts intestinal epithelial barrier function via altering expression of key tight junction and adherens junction proteins. Cell Microbiol 20, e12830. [PubMed: 29444370]

Lamarque MH, Papoin J, Finizio AL, Lentini G, Pfaff AW, Candolfi E, Dubremetz JF, and Lebrun M. (2012). Identification of a new rhoptry neck complex RON9/RON10 in the Apicomplexa parasite Toxoplasma gondii. PLoS One7, e32457. [PubMed: 22427839]

Laporta MZ, Silva ML, Scaletsky IC, and Trabulsi LR (1986). Plasmids coding for drug resistance and localized adherence to HeLa cells in enteropathogenic Escherichia coli O55:H- and O55:H6. Infect Immun 51, 715–717. [PubMed: 3510986]

Le Roch KG, Zhou YY, Blair PL, Grainger M, Moch JK, Haynes JD, De la Vega P, Holder AA, Batalov S, Carucci DJ, et al. (2003). Discovery of gene function by expression profiling of the malaria parasite life cycle. Science 301, 1503–1508. [PubMed: 12893887]

Lendner M, and Daugschies A. (2014). Cryptosporidium infections: molecular advances. Parasitology141, 1511–1532. [PubMed: 24679517]

Lima TS, and Lodoen MB (2019). Mechanisms of Human Innate Immune Evasion by Toxoplasma gondii. Front Cell Infect Microbiol 9, 103. [PubMed: 31041194]

Lin YH, Zhen YY, Chien KY, Lee IC, Lin WC, Chen MY, and Pai LM (2017). LIMCH1 regulates nonmuscle myosin-II activity and suppresses cell migration. Mol Biol Cell 28, 1054–1065. [PubMed: 28228547]

Liu X, Yuan H, Zhou J, Wang Q, Qi X, Bernal C, Avella D, Kaifi JT, Kimchi ET, Timothy P, et al. (2021). LMO7 as an Unrecognized Factor Promoting Pancreatic Cancer Progression and Metastasis. Frontiers in Cell and Developmental Biology 9.

Lu HL, Wang JB, Brown MA, Euerle C, and St Leger RJ (2015). Identification of Drosophila Mutants Affecting Defense to an Entomopathogenic Fungus. Scientific reports 5, 12350. [PubMed: 26202798]

Mauzy MJ, Enomoto S, Lancto CA, Abrahamsen MS, and Rutherford MS (2012). The Cryptosporidium parvum transcriptome during in vitro development. PLoS One 7, e31715. [PubMed: 22438867]

McNair NN, Bedi C, Shayakhmetov DM, Arrowood MJ, and Mead JR (2018). Inflammasome components caspase-1 and adaptor protein apoptosis-associated speck-like proteins are important in resistance to Cryptosporidium parvum. Microbes Infect 20, 369–375. [PubMed: 29842985]

Mueller C, Klages N, Jacot D, Santos JM, Cabrera A, Gilberger TW, Dubremetz JF, and Soldati-Favre D. (2013). The Toxoplasma Protein ARO Mediates the Apical Positioning of Rhoptry Organelles, a Prerequisite for Host Cell Invasion. Cell Host & Microbe13, 289–301. [PubMed: 23498954]

Mueller C, Samoo A, Hammoudi PM, Klages N, Kallio JP, Kursula I, and Soldati-Favre D. (2016). Structural and functional dissection of Toxoplasma gondii armadillo repeats only protein. J Cell Sci129, 1031–1045. [PubMed: 26769898]

Nakamura H, Mukai M, Komatsu K, Tanaka-Okamoto M, Itoh Y, Ishizaki H, Tatsuta M, Inoue M, and Miyoshi J. (2005). Transforming growth factor-beta1 induces LMO7 while enhancing the invasiveness of rat ascites hepatoma cells. Cancer Lett220, 95–99. [PubMed: 15737692]

Ojcius DM, Perfettini JL, Bonnin A, and Laurent F. (1999). Caspase-dependent apoptosis during infection with Cryptosporidium parvum. Microbes Infect1, 1163–1168. [PubMed: 10580271]

Ooshio T, Irie K, Morimoto K, Fukuhara A, Imai T, and Takai Y. (2004). Involvement of LMO7 in the association of two cell-cell adhesion molecules, nectin and E-cadherin, through afadin and alpha-actinin in epithelial cells. J Biol Chem279, 31365–31373. [PubMed: 15140894]

Ostrovska K, and Paperna I. (1990). Cryptosporidium sp. of the starred lizard Agama stellio: ultrasturcture an life cycle. Parasitol Res76, 712–720.

Rauch I, Deets KA, Ji DX, von Moltke J, Tenthorey JL, Lee AY, Philip NH, Ayres JS, Brodsky IE, Gronert K, et al. (2017). NAIP-NLRC4 Inflammasomes Coordinate Intestinal Epithelial Cell Expulsion with Eicosanoid and IL-18 Release via Activation of Caspase-1 and −8. Immunity 46, 649–659. [PubMed: 28410991]

Ribet D, and Cossart P. (2015). How bacterial pathogens colonize their hosts and invade deeper tissues. Microbes Infect17, 173–183. [PubMed: 25637951]

Riedl J, Crevenna AH, Kessenbrock K, Yu JH, Neukirchen D, Bista M, Bradke F, Jenne D, Holak TA, Werb Z, et al. (2008). Lifeact: a versatile marker to visualize F-actin. Nature Methods 5, 605–607. [PubMed: 18536722]

Sasaki M, Tsuji N, Furuya M, Kondoh K, Kamagata C, Kobayashi D, Yagihashi A, and Watanabe N. (2003). PCD1, a novel gene containing PDZ and LIM domains, is overexpressed in human breast cancer and linked to lymph node metastasis. Anticancer Res23, 2717–2721. [PubMed: 12894564]

Sateriale A, Gullicksrud JA, Engiles JB, McLeod BI, Kugler EM, Henao-Mejia J, Zhou T, Ring AM, Brodsky IE, Hunter CA, et al. (2021). The intestinal parasite Cryptosporidium is controlled by an enterocyte intrinsic inflammasome that depends on NLRP6. Proc Natl Acad Sci U S A 118.

Sateriale A, Pawlowic M, Vinayak S, Brooks C, and Striepen B. (2020). Genetic Manipulation of Cryptosporidium parvum with CRISPR/Cas9. Methods Mol Biol2052, 219–228. [PubMed: 31452165]

Sateriale A, Slapeta J, Baptista R, Engiles JB, Gullicksrud JA, Herbert GT, Brooks CF, Kugler EM, Kissinger JC, Hunter CA, et al. (2019). A Genetically Tractable, Natural Mouse Model of Cryptosporidiosis Offers Insights into Host Protective Immunity. Cell Host Microbe 26, 135–146 e135. [PubMed: 31231045]

Stauffer TP, Ahn S, and Meyer T. (1998). Receptor-induced transient reduction in plasma membrane PtdIns(4,5)P2 concentration monitored in living cells. Curr Biol8, 343–346. [PubMed: 9512420]

Stenberg P, Norinder U, Luthman K, and Artursson P. (2001). Experimental and computational screening models for the prediction of intestinal drug absorption. J Med Chem44, 1927–1937. [PubMed: 11384238]

Suarez C, Lentini G, Ramaswamy R, Maynadier M, Aquilini E, Berry-Sterkers L, Cipriano M, Chen AL, Bradley P, Striepen B, et al. (2019). A lipid-binding protein mediates rhoptry discharge and invasion in Plasmodium falciparum and Toxoplasma gondii parasites. Nat Commun 10, 4041. [PubMed: 31492901]

Tanaka R, Miyata S, Yamaguchi M, and Yoshida H. (2019). Role of the smallish gene during Drosophila eye development. Gene684, 10–19. [PubMed: 30359736]

Tandel J, English ED, Sateriale A, Gullicksrud JA, Beiting DP, Sullivan MC, Pinkston B, and Striepen B. (2019). Life cycle progression and sexual development of the apicomplexan parasite Cryptosporidium parvum. Nat Microbiol4, 2226–2236. [PubMed: 31477896]

Tetley L, Brown SM, McDonald V, and Coombs GH (1998). Ultrastructural analysis of the sporozoite of Cryptosporidium parvum. Microbiology 144 ( Pt 12), 3249–3255. [PubMed: 9884216]

Tonkin ML, Roques M, Lamarque MH, Pugniere M, Douguet D, Crawford J, Lebrun M, and Boulanger MJ (2011). Host Cell Invasion by Apicomplexan Parasites: Insights from the Co-Structure of AMA1 with a RON2 Peptide. Science 333, 463–467.

Ugalde-Silva P, Gonzalez-Lugo O, and Navarro-Garcia F. (2016). Tight Junction Disruption Induced by Type 3 Secretion System Effectors Injected by Enteropathogenic and Enterohemorrhagic Escherichia coli. Front Cell Infect Microbiol6, 87. [PubMed: 27606286]

Valentini E, Cherchi S, Possenti A, Dubremetz JF, Pozio E, and Spano F. (2012). Molecular characterisation of a Cryptosporidium parvum rhoptry protein candidate related to the rhoptry neck proteins TgRON1 of Toxoplasma gondii and PfASP of Plasmodium falciparum. Molecular and Biochemical Parasitology183, 94–99. [PubMed: 22343414]

Vinayak S, Pawlowic MC, Sateriale A, Brooks CF, Studstill CJ, Bar-Peled Y, Cipriano M, and Striepen B. (2015). Genetic Modification of the Diarrheal Pathogen Cryptosporidium Parvum. American Journal of Tropical Medicine and Hygiene93, 587–587.

Wang K, Peng ED, Huang AS, Xia D, Vermont SJ, Lentini G, Lebrun M, Wastling JM, and Bradley PJ (2016). Identification of Novel O-Linked Glycosylated Toxoplasma Proteins by Vicia villosa Lectin Chromatography. PLoS One 11, e0150561. [PubMed: 26950937]

Wetzel DM, Schmidt J, Kuhlenschmidt MS, Dubey JP, and Sibley LD (2005). Gliding motility leads to active cellular invasion by Cryptosporidium parvum sporozoites. Infection and Immunity 73, 5379–5387. [PubMed: 16113253]

Yang X, Boehm JS, Yang X, Salehi-Ashtiani K, Hao T, Shen Y, Lubonja R, Thomas SR, Alkan O, Bhimdi T, et al. (2011). A public genome-scale lentiviral expression library of human ORFs. Nat Methods 8, 659–661. [PubMed: 21706014]

Zhang H, Guo F, and Zhu G. (2012). Involvement of host cell integrin alpha2 in Cryptosporidium parvum infection. Infect Immun80, 1753–1758. [PubMed: 22354032]

Zhang H, Guo F, and Zhu G. (2015). Cryptosporidium Lactate Dehydrogenase Is Associated with the Parasitophorous Vacuole Membrane and Is a Potential Target for Developing Therapeutics. PLoS Pathog11, e1005250. [PubMed: 26562790]

**Highlights (should be less than 85 characters in length including space)**

- Live imaging of *Cryptosporidium* invasion shows host actin and membrane modification
- Screen identifies and validates the first 6 *Cryptosporidium* rhoptry bulb proteins
- ROP1 is injected into the host cell and binds LMO7, a host cytoskeletal modulator
- Genetic ablation of ROP1 or LMO7 impacts on parasite infection *in vivo*

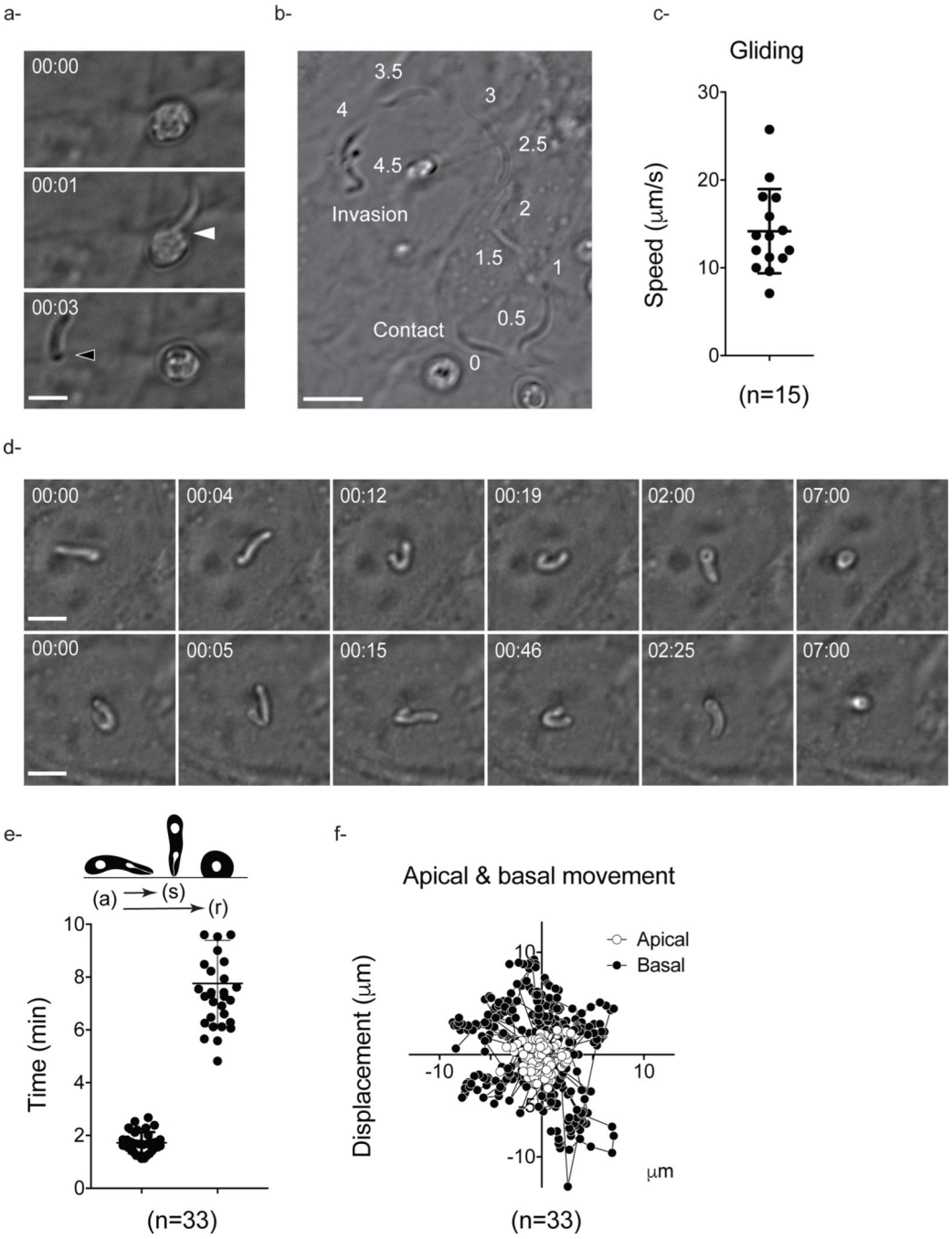


**Figure 1: Invasion of HCT8 cells by *Cryptosporidium* sporozoites**

**a.** Frames of video 1 showing a sporozoite emerging from oocyst and within 3 s attaching to a host cell to invade. White arrow head labels the sporozoite exiting the oocyst, the black arrow head labels the point of attachment onto the host cell. Scale bar 5μm. **b.** Kinogram of sporozoite gliding on cells, a stitched composite of 10 video frames numbers indicates s from initial contact (mean speed 18μm/s). Scale bar 10μm. **c.** Quantification of 15 gliding events (mean speed of 14.2μm/s). **d.** Frames of video 2 showing two sporozoites during invasion. Apical contact is followed by initial contortion, straightening, and rounding into

trophozoite. Scale bar 5μm; time displayed in min and s. e. Quantification of the timing of 33 invasion events from attachment (a) to straightening (t) (mean= 1:43 min) and attachment (a) to complete trophozoite transformation (r) (mean=7:42 min). f. Displacement of the apical and basal ends of 33 recorded invading parasites over the first 275 s of invasion.

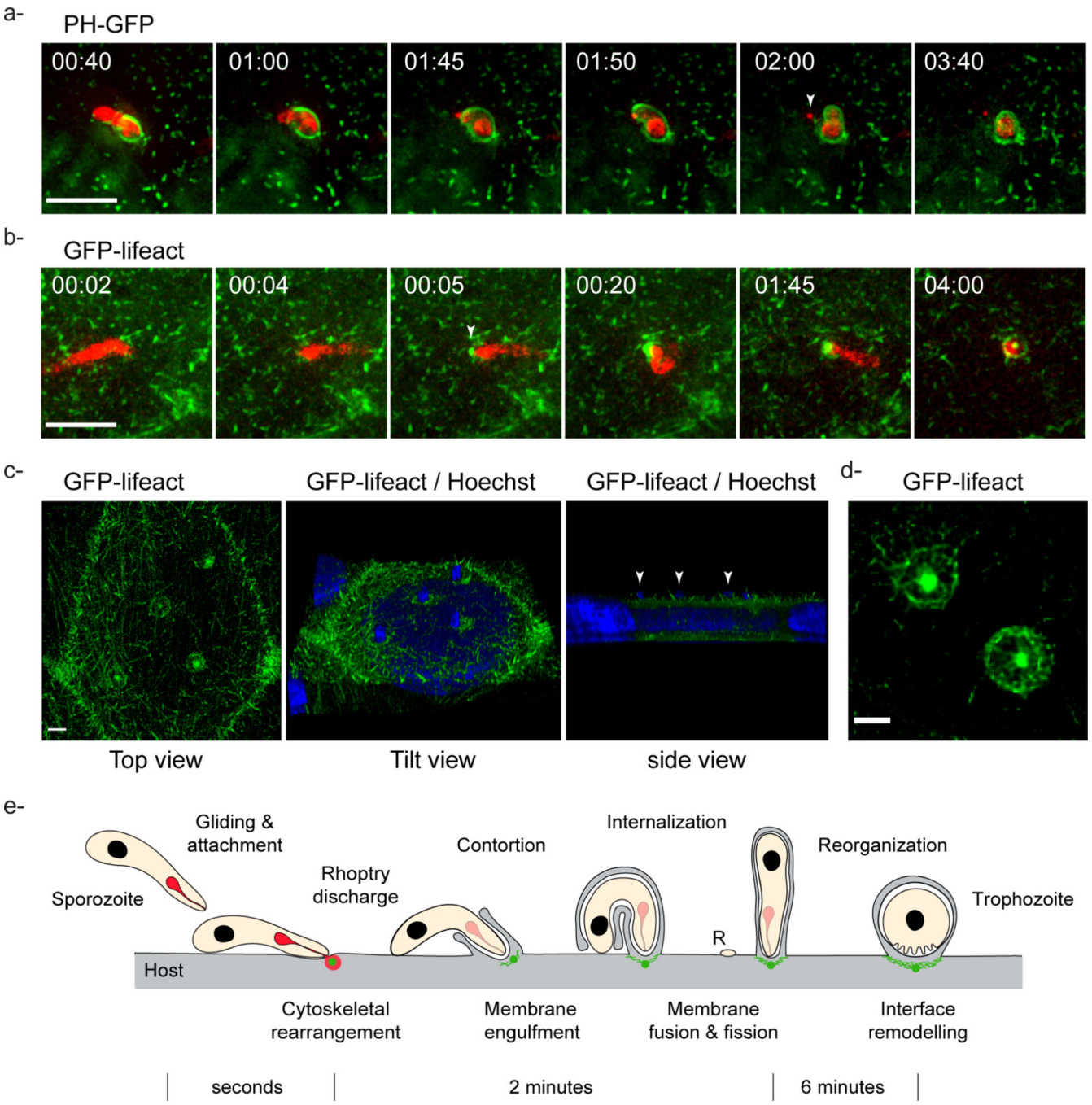


**Figure 2: Modification of host membrane and cytoskeleton during *Cryptosporidium* invasion**

**a.** Frames of video 3 showing *C. parvum* TdTomato (red) invading a HCT8 cell expressing GFP-PLCdelta-PH (green) on its plasma membrane. Arrowhead highlights residual parasite material following fission. **b.** Frames of video 4 showing *C. parvum* TdTomato invading a host cell expressing lifeact (green). Arrowhead highlights initial actin polymerization. a and b. Scale bars 5μm; time displays in min and s. **c.** Projections of confocal microscopy image stack recorded 2 h after addition of oocysts showing host actin pedestals formed at the infection site (lifeact, green; DNA, blue). Arrowheads highlight parasite nuclei.

Scale bar 1μm. Tilt view of an additional infected cell available in video 5. **d.** Stimulated emission depletion microscopy micrograph of lifeact at the infection site. Note actin basket with central density. **e.** Model of *Cryptosporidium* invasion depicting parasite and host events from an extracellular parasite to an intracellular trophozoite. The sporozoite glides and attaches to the host cell. Apical contact within seconds results in induction of host actin polymerization and rhoptry discharge (figure S2d). Over two minutes, the parasite is engulfed by host membranes which coincides with parasite contortion. During the next six minutes, the parasite will round up and the actin pedestal elaborates into a cup-like structure. A residue (R) of parasite material remains at the host surface suggesting a membrane fission event. The rhoptry is shown in red, actin in green.

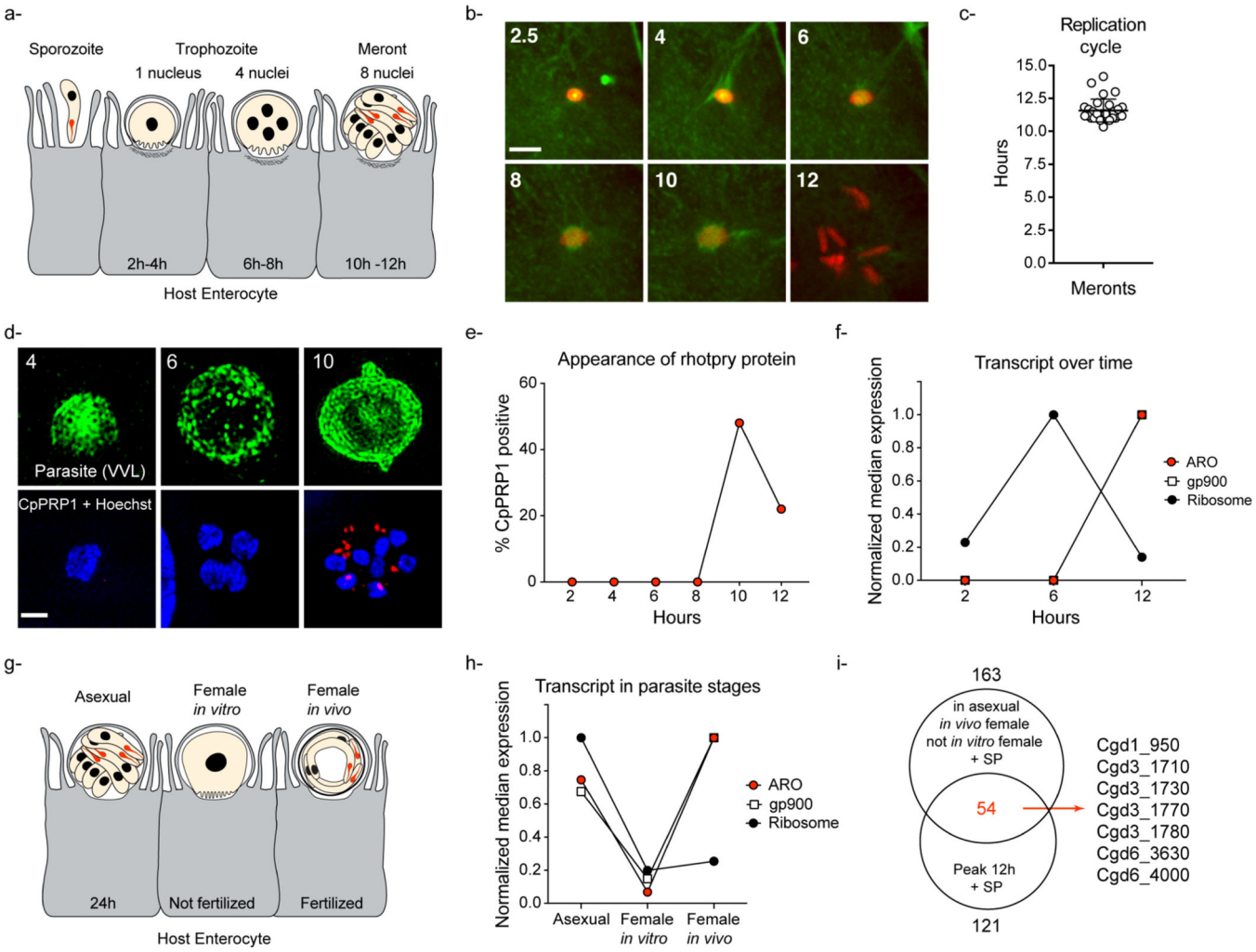


**Figure 3: Rhoptry biogenesis occurs at the end of the schizogony cycle**

**a.** Schematic view of the rhoptry (labelled in red) at different stages of asexual replication. **b.** Frames of a 12h video of asexual replication of *C. parvum* TdTomato (red) in HCT8 cells expressing lifeact (green). Note egress of 8 merozoites in last time point. Full set available as video 6. Scale bar 5μm. **c.** Quantification of intracellular development of *Cryptosporidium* through video-microscopy, each symbol corresponds to an independent parasite cycle (Mean= 11.5 h, STD=0.86h, n=29). **d.** Representative super-resolution micrographs of intracellular stages over a time course of infection. Rhoptries were labeled for CpPRP1 (red), parasitophorous vacuole with VVL-FITC (green), and nuclei with Hoechst (blue). Time displays in h, scale bar 1μm. **e.** Quantification of the time course of rhoptry biogenesis measured by IFA every 2h for 12h and converted to percent of total VVL detected parasites. Note peak of CpPRP1 rhoptry labelling at 10h and 12h post infection. **f.** qRT-PCR of transcript abundance of *C. parvum* homolog of TgARO (cgd2_370) over infection time. ARO transcript, like the micronemal protein gp900, peaks at 12 hours while ribosomal proteins (e.g. cgd8_2870) are transcribed earlier (data replotted from (Mauzy et al., 2012)). **g.** Graphic representation of rationale for use of stage specific transcriptome data, rhoptry proteins (red) are expected to be expressed in *in vivo* females and in culture asexual stages

but not in culture females as those do not undergo sporogony due to lack of fertilization **h.** RNAseq of transcript abundance of TgARO (cgd2_370) in different stages. ARO transcript, like the micronemal protein gp900, is detected in asexual and female stages *in vivo* while the ribosomal protein is low in females *in vivo* (data replotted from (Tandel et al., 2019)). **i.** Filtering scheme for candidate rhoptry proteins, a list is available as table S1.

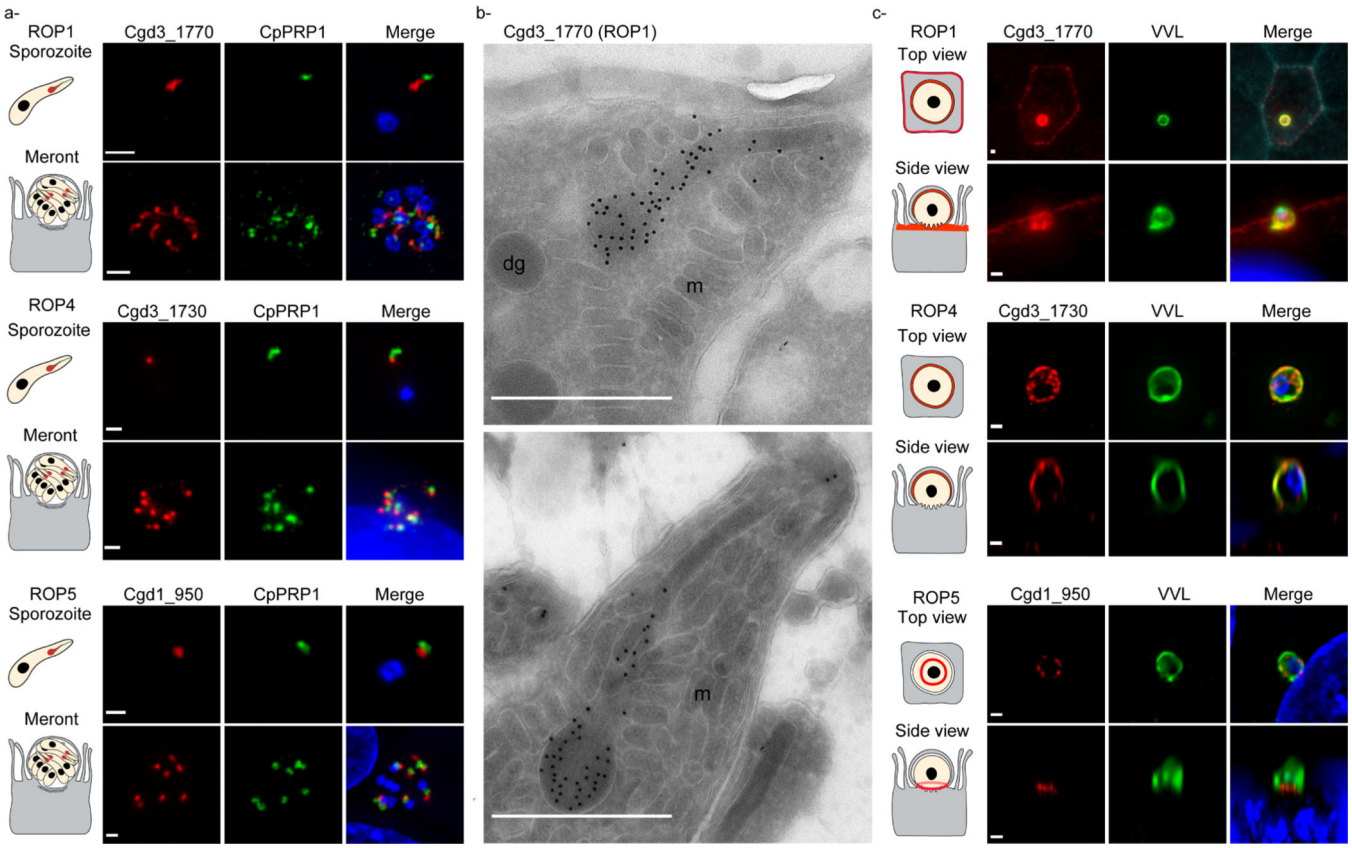


**Figure 4: Localization of *C. parvum* rhoptry bulb proteins before and after secretion**

**a.** Immunofluorescence of extracellular sporozoites (top) and in eight nuclei meronts (bottom) for three transgenic *C. parvum* lines (respective tagged genes are indicated for each panel, three additional tagged proteins are shown in figure S3). HA label (red) was found in close proximity but non-overlapping with the rhoptry neck marker CpPRP1 (green). Nuclei are labelled with Hoechst in blue. Scale bar 1μm. **b.** Cryo-immunoelectron micrographs of the apical ends of two representative sporozoites expressing cgd3_1770-HA labelled with anti-HA and protein A-gold. The gold particles accumulate over the bulbus part of the rhoptry. m, microneme; dg, dense granule. Scale bar 500nm. **c.** Immunofluorescence of tagged strains in trophozoite stage, 2h after invasion (which we found representative for the entire intracellular development), with HA in red, VVL in green, Hoechst in blue, and for cgd3_1770 top panel actin in cyan. Scale bar 1μm. Cgd3_1770 accumulates at the PV but is also identified at the periphery of the host cell; cgd3_1730 accumulates at the parasitophorous vacuole; cgd1_950 assumes a ring-like localization at the interface of host and parasite best appreciated in side view.

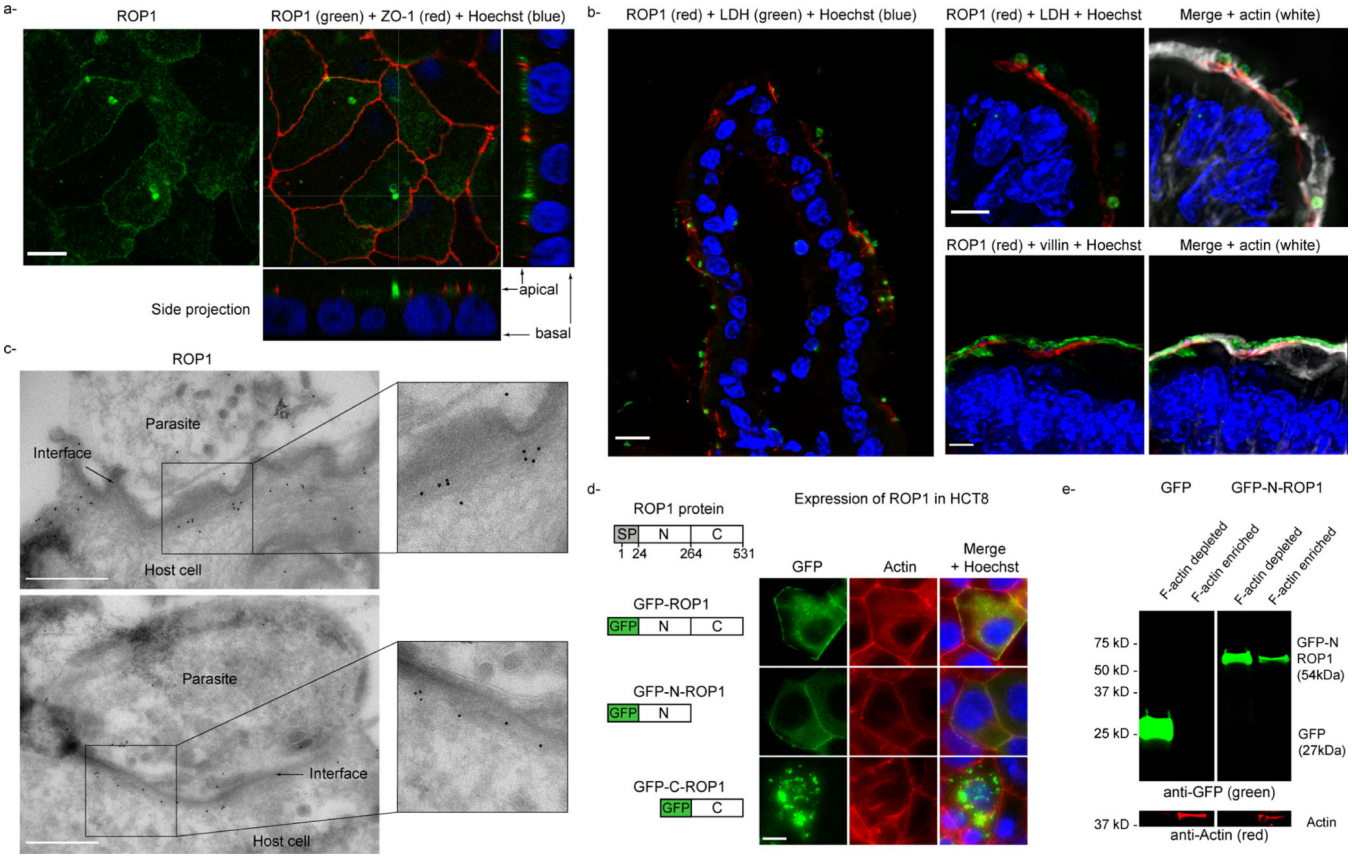


**Figure 5: ROP1 is injected into the host cell and apically restricted *in vitro* and *in vivo***

**a.** Immunofluorescence of ROP1-HA in a fully differentiated Caco2 monolayer. ROP1, in green, is secreted into the host cell and localized to the apical side of the polarized cells as well as at the infection site. ZO-1 is an apical tight junction marker shown in red, Hoechst in blue. Scale bar 10μm. Tilt view available in video 7 with actin in white. **b.** Immunofluorescence of a histological section of the small intestine of a mouse infected with ROP1-HA parasites. Left: ROP1 in red, parasites in green (LDH) and nuclei in blue (Hoechst). Scale bar 10μm. Top right: ROP1 in red, parasites (LDH) in green, and actin in white. ROP1 is found only in infected cells and is apically restricted. Scale bar 5μm. Bottom right: Immunofluorescence showing the localization of ROP1 in red, villin (a marker for apical microvilli) in green and actin in white. ROP1 accumulates at the apical side of the enterocytes but not in the microvilli. Scale bar 5μm. **c.** Cryo-immunoelectron micrographs of HCT8 cells 2 h after infection with ROP1-HA (gold) parasites. The gold particles accumulate inside the host cell, at the interface with the parasite, over a region rich in filaments corresponding to actin. Scale bar 500nm. **d.** Ectopic expression of ROP1 in translational fusion with GFP in HCT8 cells. Constructs included the full ROP1 coding sequence (omitting its signal peptide), an N- and C-terminal deletions. Green corresponds to GFP-ROP1, actin in red and Hoechst is in blue. Scale bar 10μm. e. Western blot analysis of fractionation experiment. Note accumulation of GFP-N-ROP1 in the F-actin enriched fraction and compared to the GFP-only control, which remained in the F-actin depleted fraction. GFP in green, actin in red.

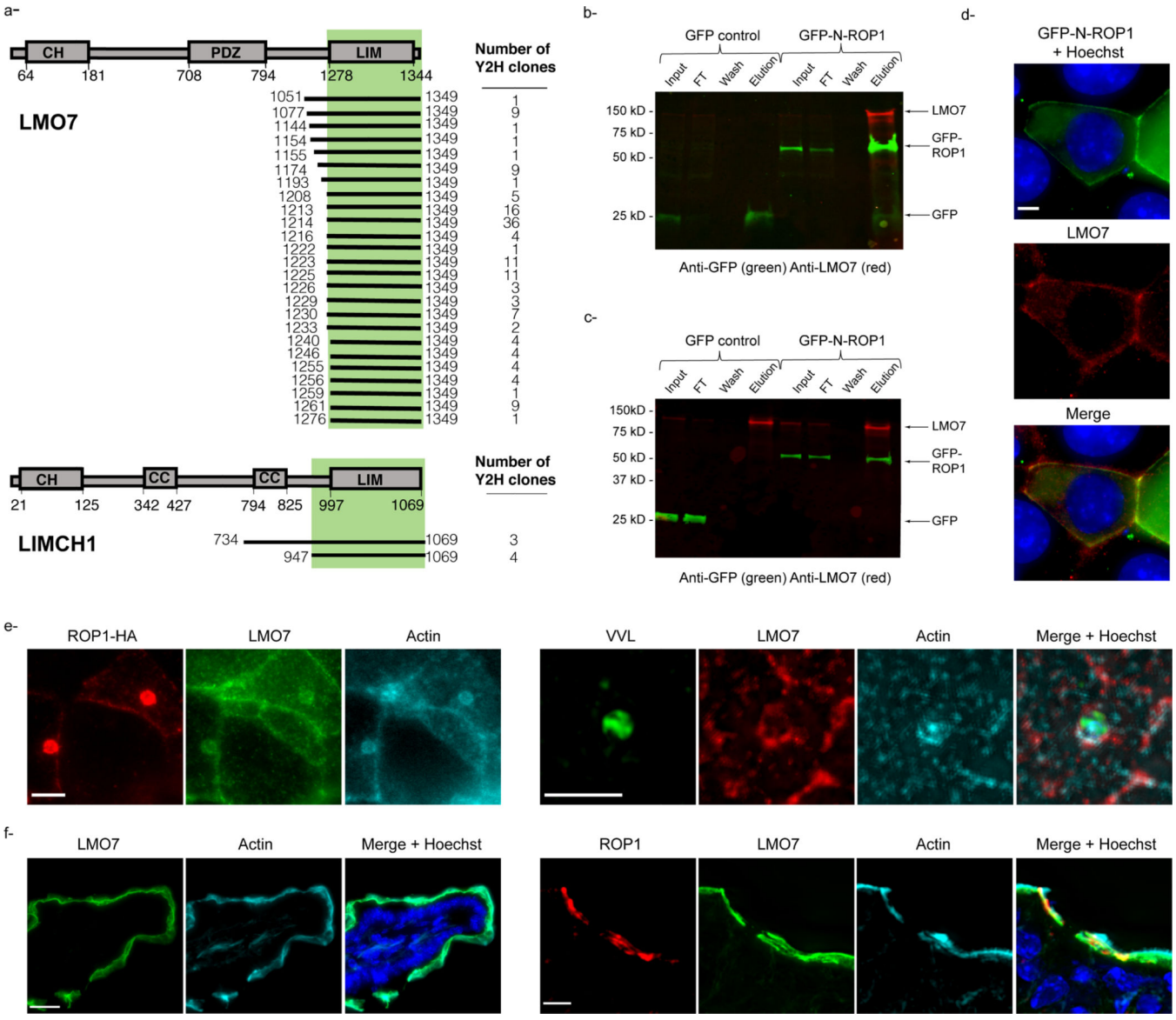


**Figure 6: ROP1 targets LMO7 a component of the terminal web in human and mouse epithelial cells**

**a.** Multiple sequence alignment of the results of a yeast-two hybrid screen using the N-terminal part of ROP1 as bait against a library derived from multiple lines of human intestinal epithelial cells. Unique clones mapping to LMO7 or LIMCH1 are shown along with number of times each clone was observed. Note that all clones encompass and by-and-large are restricted to the LIM domain. **b.** Western blot of a GFP immunoprecipitation experiment using HCT8 cells expressing GFP or GFP-N-ROP1. LMO7 is recovered only in the presence of ROP1. **c.** Reverse immunoprecipitation experiment using anti-LMO7 antibodies coupled to protein G beads on similarly transfected cells. LMO7 pull down recovers GFP-N-ROP1 but not GFP alone. Anti-GFP in green, anti-LMO7 in red. **d.** Immunofluorescence of HCT8 expressing GFP-N-ROP1 (green), LMO7 in red and Hoechst in blue. Note the colocalization of LMO7 with GFP-N-ROP1, scale bar 5μm. **e.** Left,

immunofluorescence of HCT8 cells infected with ROP1-HA parasites. ROP1 in red, LMO7 in green, actin in cyan, and Hoechst in blue. Right, immunofluorescence of infected cells, LMO7 (red), actin (cyan), parasite (VVL, green). Scale bar 5μm. **f.** Immunofluorescence of histological sections of the ileum of uninfected (left) and ROP1-HA parasite infected (right) mice. LMO7, in green, and actin, in cyan, colocalize at the apical brush of the enterocytes. ROP1-HA labeling coincides with LMO7 in infected cells. Hoechst is in blue. Scale bar, 20μm left, 5μm right.

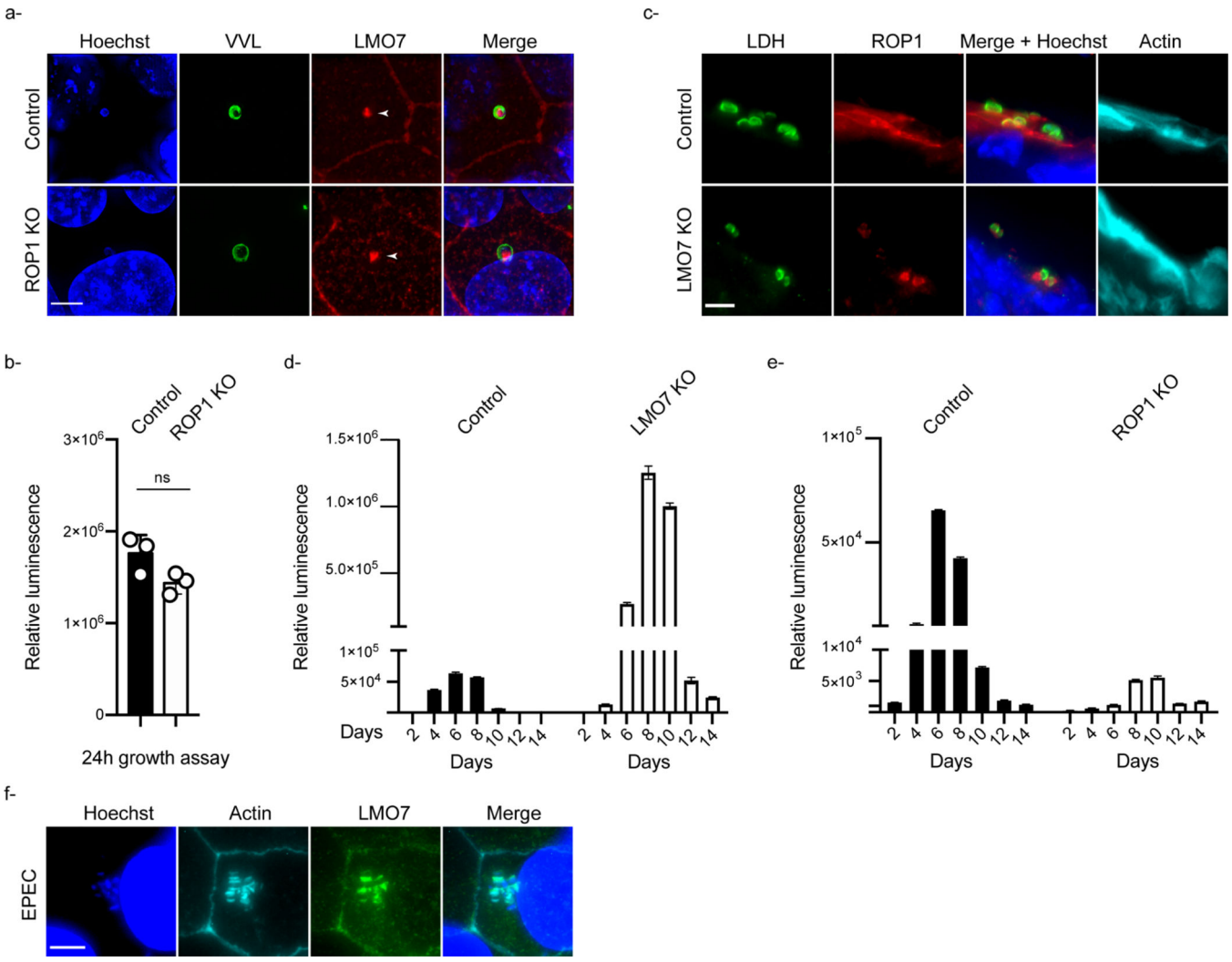


**Figure 7: Loss of ROP1 reduces parasite burden *in vivo* while loss of host LMO7 enhances infection**

**a.** Immunofluorescence of HCT8 cells infected with WT control (ROP1-HA) and ROP1 KO parasites. Note that LMO7 is present at the infection site in absence of ROP1 (arrowhead). Hoechst in blue, VVL in green and LMO7 in red. Scale bar 5μm. **b.** Luciferase-based growth assay of ROP1-HA control and mutant ROP1 KO parasites in HCT8 cell culture. No significant difference was observed. n=3. **c.** Immunofluorescence of histological sections of the intestines of C57BL/6 WT and LMO7 KO mice infected with ROP1-HA parasites. Recruitment of ROP1 to the apical terminal web of enterocytes is lost in the absence of LMO7. ROP1 in red, actin in cyan, and Hoechst in blue. Scale bar 5μm. **d.** C57BL/6 WT and LMO7 KO mice were infected with *C. parvum* and parasite burden was measured following fecal luciferase activity. Mice showed a 15.3-fold increase of infection (area under the curve, representative example shown) in absence of LMO7. 3 to 4 mice per group, 3 independent biological repeats (15.2, 18.3, and 15.3-fold, respectively). n=3. **e.** Mice were infected with control ROP1-HA and mutant ROP1 *C. parvum* and parasite shedding was quantified every two days by measuring fecal luciferase activity. ROP1 KO parasites produced an 8.7-fold lower burden when comparing the area under the curve to

WT (representative dataset shown here). 3 mice per group, 3 independent biological repeats (8.7, 24, and 7.2-fold, respectively). n=3. Immunocompetent mice are resistant to *C. parvum* infection, mice in e. were *ifnγ* $^{-/-}$ and in d. injected with anti-IFNγ antibody as detailed in the Materials and Methods. **f.** Immunofluorescence of HCT8 cells infected with EPEC for 1 hour. LMO7 is recruited at the actin pedestal induced by EPEC. Actin in cyan, LMO7 in green, Hoechst in blue, scale bar 5μm.

| REAGENT or RESOURCE | SOURCE | IDENTIFIER |
|---|---|---|
| Antibodies | | |
| Anti-HA | Cell Signaling | 3724S; RRID:AB_1549585 |
| Anti-HA (for IEM) | Roche | Clone 3F10; RRID:AB_390918 |
| Anti-ZO1 | Thermo Fisher | 33–9100; RRID:AB_2533147 |
| Anti-villin | Abcam | Ab130751; RRID:AB_11159755 |
| Anti-tubulin | Abcam | Ab7291; RRID: AB_2241126 |
| Anti-actin | Santa Cruz | SC8432 clone C-2; RRID:AB_626630 |
| Anti-GFP | Invitrogen | A11122; RRID:AB_221569 |
| Anti-LMO7 | Santa Cruz | SC376807; RRID:AB_2892126 |
| Anti-LMO7 | Sigma | HPA020923; RRID:AB_1852963 |
| Anti-cp23 | LS Bio | LS-C137378–100; RRID:AB_10947007 |
| Anti-CpPRP1 | Furio Spano laboratory | (Valentini et al., 2012) |
| Anti-LDH | Guan Zhu laboratory | (Zhang et al., 2015) |
| Bacterial and virus strains | | |
| *Escherichia coli* GC5 | Genesee Scientific | 42–653 |
| Enteropathogenic *E. coli* strain 49–81 HSJ | Dieter Schifferli laboratory | (Laporta et al., 1986) |
| Critical commercial assays | | |
| Quick-DNA Fecal/Soil Microbe Kit | Zymo Research | Cat# D6010 |
| GFP-trap magnetic beads | chromotek | 90122001MA |
| Dynabeads Protein G | Invitrogen | 10004D |
| lipofectamine | Thermo Fisher | L3000015 |
| BS3 conjugation buffer | Thermo Fisher | 21580 |
| RNeasy Plus mini kit | Quiagen | 74134 |
| SuperScript IV First-Strand synthesis System | Thermo Fisher | 18091050 |
| Experimental models: Cell lines | | |
| HCT8 | ATCC | CCL-244 |
| Caco2 | ATCC | HTB-37 |
| HEK293 | ATCC | CRL-1573 |
| Experimental models: Organisms/strains | | |
| *Cryptosporidium parvum* | Bunchgrass Farms, ID | IOWA strain |
| C57BL/6 mice | Jackson Laboratory | Strain 000664 |
| *ifnγ*$^{-/-}$ mice | Jackson Laboratory | Strain 002287 |
| LMO7 KO mice | Jung-Bum Shin laboratory | (Du et al., 2019) |
| Oligonucleotides | | |
| Primers for cloning see Table S2 | This paper | N/A |
| Software and algorithms | | |

| REAGENT or RESOURCE | SOURCE | IDENTIFIER |
|---|---|---|
| PRISM | GraphPad | https://www.graphpad.com/scientific-software/prism/ |
| Volocity | Quorum Technologies | https://quorumtechnologies.com/index.php/component/content/category/31-volocity-software |
| ImageJ | ImageJ | https://imagej.net/Welcome |
| Other | | |
| 8 well microslides | Ibidi | 80826 |
| VVL-FITC | Vector | FL1231 |
| Phalloidin | Thermo Fisher | A22287 |